

---

## A new rheological model for thixoelastic materials in subaqueous gravity driven flows

Hermidas Navid <sup>1,\*</sup>, Silva Jacinto Ricardo <sup>2</sup>, Eggenhuisen Joris T. <sup>3</sup>, Luthi Stefan M. <sup>1</sup>

<sup>1</sup> Faculty of Civil Engineering and Geosciences, TU Delft, Delft, Netherlands

<sup>2</sup> Marine Geosciences Unit, Ifremer, Brest, France

<sup>3</sup> Department of Earth Sciences, Utrecht University, Utrecht, Netherlands

\* Corresponding author : Navid Hermidas, email address : [n.hermidas@tudelft.nl](mailto:n.hermidas@tudelft.nl)

---

### Abstract :

A new viscoelastic constitutive model for subaqueous clay-rich gravity flows is presented. It is explained that for the materials which exhibit a minimum in their strain controlled flow curves the structure parameter must be a symmetric function of strain rate and stress. Therefore, the destruction of structure within the material is modeled using the dissipation energy. An expression for the elastic strain of the flowing structure is derived. The final set of equations can reproduce the viscosity bifurcation that clay suspensions may exhibit under a given load. This is explained to be important for prediction of the run-out distance of clay-rich gravity flows. The ability of the model to reproduce the general response of pasty materials to step stress and step shear rate tests is examined. The model requires four empirical parameters. A methodology is presented for obtaining these parameters and power law functions are given for their calculations for a limited rest time of 3000 seconds. The ability of the model to reproduce the rheological behavior that clay-rich suspensions exhibit under both stress and strain controlled conditions is examined using rheometry tests.

### Highlights

► A new rheological model with only four empirical parameters is presented. ► Our rheological model explains the run-out distances of clay-rich gravity flows. ► The structure parameter is a symmetric function of the strain rate and stress. ► An expression for the elastic strain of the flowing structure is derived. ► Our rheological model can reproduce the viscosity bifurcation of clay suspensions.

**Keywords** : gravity flow, thixotropy, clay suspension, viscosity bifurcation

## 1. Introduction

Clay is present in the majority of deep marine [1], coastal [2, 3], and fluvial environments [4]. For clay-rich gravity flows, presence of clay greatly influences the run-out distance and the internal structure of these flows [5, 6].

Using their inclined plane experiments, Coussot et al. [7, 8] showed that under a given load, clay suspensions experience viscosity bifurcation, i.e., they either stop flowing altogether or experience a discontinuous decrease in their viscosity depending on their structural state at the time of the applied stress. They concluded that, for strain controlled measurements, stable flows can occur only when the shear rate is above a critical value. For smaller shear rates the material either fractures or shows shear banding instabilities [9]. These experiments also showed that if a clay-water suspension with a given thickness begins to flow on a certain slope, it will stop only when the thickness is reduced dramatically or when the slope is decreased considerably. This

---

\*Email address for correspondence: N.Hermidas@tudelft.nl

phenomenon is a consequence of the existence of two yield stresses. One which governs the initiation of the flow from rest and is known as the static yield stress,  $\tau_y$ , and the other which governs the abrupt stoppage/freezing of the flow and is known as the dynamic or critical yield stress,  $\tau_c$ . The static yield stress is larger than the critical yield stress and the difference between the two is the factor which governs the run-out distance of clay-water suspensions. The model which will be presented here can capture both the static and the critical yield stresses of clay-water suspensions, and therefore, can be used to accurately simulate the run-out distance of gravity flows.

The most complete anatomy of subaqueous clay-rich gravity flows is composed of three vertically stacked layers [10]. These three regions are characterized in Figure 1(a), which depicts the velocity profile of a clay-rich sediment gravity flow during small scale flume experiments [10].

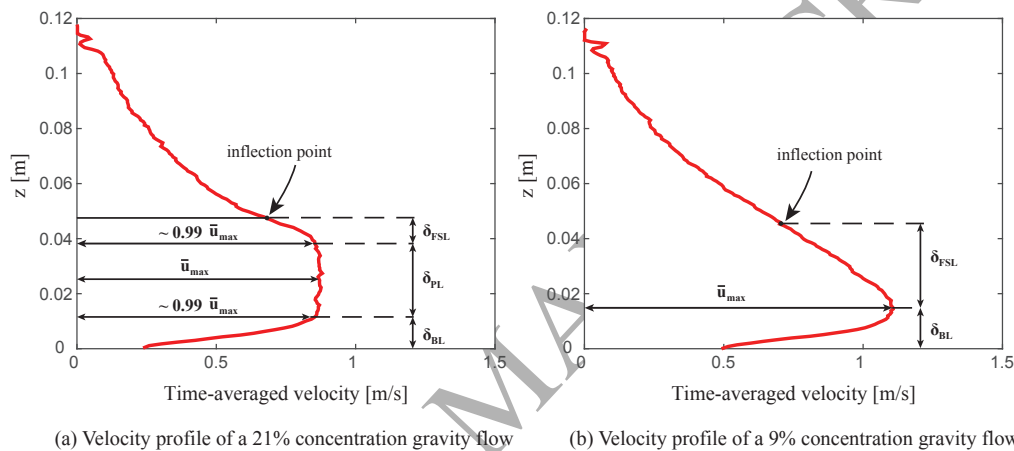


Figure 1: Free shear layer,  $\delta_{FSL}$ , plug layer,  $\delta_{PL}$ , and boundary layer,  $\delta_{BL}$ , regions of sediment gravity flows captured using an Ultrasonic Doppler Velocity probe [10].

The density and velocity gradients that exist on the interface between the sediment flow and the overlying water result in a dilute mixing layer known as the free shear layer. Due to low sediment concentration, the fluid within this layer behaves similar to a Newtonian fluid. The free shear layer is stacked on top of a layer referred to as the plug layer. The behavior of the mixture within this layer resembles that of a gel-like suspension whose yield stress is reached on the interface where the free shear layer and the plug layer meet. The existence and size of the plug layer is dependent on the sediment concentration, and for dilute sediment gravity flows it disappears, as shown in Figure 1(b). Due to the no slip condition between the sediment flow and the bed, the plug layer in the vicinity of the bed is liquefied, producing a third layer known as the boundary layer. The fluid within this layer behaves as a viscoelastic fluid.

Modeling approaches for these flow structures are problematic due to the complex behavior of clay-water suspensions. Clay particles are flat platelets with electrostatically charged surfaces. Once immersed in high concentrations (higher than the ‘gelling’ concentration) in a medium such as water, they can form two types of structures, namely, the ‘card-house flocs’ and ‘card-pack aggregates’ [11]. Presence of these structures are characteristic of many clay-water suspensions which exhibit viscoelastic, yield, shear thinning, and thixotropic behavior [12].

Thixotropy is generally viewed as the time dependent decrease in the apparent viscosity of a

41 fluid under shear due to the break down of the structure [8]. Recovery of a damaged structure  
42 ensues once shearing is removed. The concept of simultaneous break down and build up of  
43 structure was first discussed by Goodeve [13]. Subsequent models of Moore [14], Hahn et al.  
44 [15], and Peter [16] aimed at capturing these simultaneous processes by a rate equation for a  
45 scalar structure parameter that is incorporated in the constitutive model. Generalization of these  
46 models for the special case of steady, homogeneous, incompressible, irrotational flows, came  
47 following the work of Rivlin [17, 18, 19, 12, 20]. For more general flows, different variations of  
48 these models are usually considered where various material characteristics such as yield stress  
49 [21, 22], elastic modulus, and/or viscosity are considered to be functions of the structure pa-  
50 rameter [23, 24, 25, 26, 27, 28]. These functions are generally constructed in such a way as to  
51 reproduce the overall behavior of the material.

52 In contrast to this group of models, which are based on the bulk rheological behavior of the mate-  
53 rial, a separate branch has evolved over the years which adopts a microstructural approach. The  
54 constitutive relations in these models are emergent from the physical considerations regarding  
55 the interactions between the material's microstructural constituents [29, 30, 31, 32]. While the  
56 level of abstraction that these models possess and their added intuition from the microstructural  
57 approach is appealing, considerable mathematical manipulation is usually required to express  
58 them in terms of macroscopic variables. Therefore, they have not often been employed to de-  
59 scribe experimental data sets. The bulk rheological models on the other hand, such as those of  
60 Mujumdar et al. [33] or Dullaert and Mewis [34], are written explicitly in terms of the bulk  
61 parameters and are therefore easier to employ in engineering applications.

62 Nonetheless, construction of such bulk models can suffer from ambiguities regarding how vari-  
63 ous relations should be constructed. One ambiguity has to do with the way the structure model is  
64 formulated. For instance, the destruction of structure in such models has been related to various  
65 invariants of the deviatoric stress and/or the strain rate tensors depending on the material and  
66 the flow field characteristics [27]. Here we will remove this ambiguity by resorting to physical  
67 symmetry arguments.

68 In this study a new rheological model is presented which can be used for modeling clay-rich  
69 gravity flows. In order to capture the anatomy of these flows, from the outset a constitutive  
70 model is favored that can reproduce the creep behavior of the plug layer, the yielding at the base  
71 of the plug, and the visco-elastic behavior within the boundary layer. The Kelvin-Voigt model is  
72 here considered very applicable for the elastic solid and the yield regimes, and suitable for the  
73 viscous fluid regime. Therefore, similar to the approach taken by Mujumdar et al. [33], the total  
74 stress is split into an elastic and a viscous part. However, in contrast to their approach, an ex-  
75 pression for the elastic strain of the flowing structure is not assumed. Instead, such an expression  
76 is derived based on the structure model and by assuming spring like interactions between clay  
77 particles at the micro scale. This reduces the number of empirical parameters required by the  
78 model. Generation and destruction of structure is accounted for using a structure model based  
79 on the model of Yziquel et al. [27].

80 We will discuss how the final equations capture the viscosity bifurcation and the yielding and  
81 freezing behavior that clay suspensions display under a given load. This is important for accu-  
82 rate prediction of the run-out distance of gravity flows. The most general flow curves which are  
83 allowed by the model are discussed. The model response to constant stress and constant shear  
84 rate inputs are analyzed [28, 35, 36, 34].

85 The final constitutive model requires four empirical parameters. A methodology is presented  
86 for obtaining these parameters and power law functions are give for their calculation, assuming  
87 complete structure recovery within a limited amount of rest time. We will show that the model is

88 capable of reproducing the rheological behavior that clay-rich suspensions may exhibit in both  
 89 stress and strain controlled flow conditions which exist within the free shear and boundary layers  
 90 of clay-laden environmental flows. This is achieved by comparing the output of the model with  
 91 stress and strain controlled measurements obtained from rheometry tests.

## 92 2. Rheological model

### 93 2.1. Connecting micro scale behavior to a macro scale model

94 At very short distances two clay particles exert a repulsive force on each other (Born re-  
 95 pulsion). At longer distances, this repulsive force is overcome by Van der Waals attraction and  
 96 therefore two clay particles attract each other. In the absence of other forces, the addition of these  
 97 two forces results in an equilibrium distance corresponding to the balance of Born repulsion with  
 98 Van der Waals attraction [37, 38]. A net repulsive force is generated when the particles are  
 99 brought inside the equilibrium distance, and a net attractive force when the particles are brought  
 100 outside the equilibrium distance. Therefore, at short distances the interaction of clay particles  
 101 can be modeled by springs. Although, it is known that at long distances two clay particles may  
 102 exert a net repulsive force on each other [38], here we assume that this force is weak and the  
 103 interaction can be modeled as if the spring between the particles is broken.

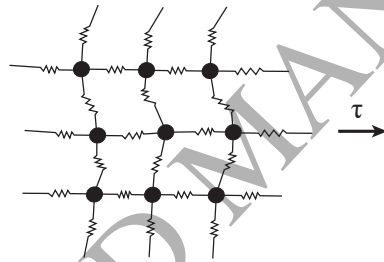


Figure 2: Clay particle network.

104 Consider a force applied to a homogeneous and isotropic network of clay particles connected  
 105 together with springs as in Figure 2. Following the homogeneity and isotropy assumptions,  
 106 away from the boundaries, the direction in which a force is applied to this network is irrelevant.  
 107 Furthermore, once equilibrium is reached the internal forces cancel out and the applied force  
 108 is counteracted by the sum of all the forces that are associated with strains in the direction of  
 109 the applied force. However, the amount of strain that the whole network experiences in the  
 110 direction of the applied force is different from the amount of strain that each individual spring  
 111 experiences. Therefore, to relate the total strain of the network to that of individual springs, we  
 112 assume that all the springs experience the same strain in the direction of the applied force as that  
 113 of the total network and instead modify their stiffnesses,  $G_i$ 's, such that the total reaction force  
 114 becomes equal to the applied external force. Thus, the complex system of springs in Figure 2  
 115 can be reduced to the one shown in Figure 3. A general form of equivalence between the model  
 116 networks is discussed by Roscoe [39], by resorting to electrical network theory.

117 The resultant strain,  $\gamma_r$ , of the system under an applied force is a residual or storage deformation  
 118 that the material exhibits or recovers in the future in a stress-free state. The liquid matrix

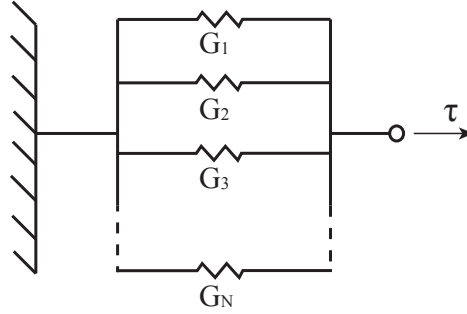


Figure 3: The simplified clay particle network model.

119 surrounding this particle network provides a viscous contribution to the total stress and is incor-  
 120 porated by adding a dashpot in parallel to the collection of springs. As stress is applied, some  
 121 connections are destroyed and some are created (this point is more thoroughly explained in the  
 122 next section). We define the modulus of elasticity,  $G_0$ , as  $\sum_{i=1}^N \frac{G_i}{N} = \frac{G_0}{N_0}$ , where  $N$  is the number  
 123 of current connections and  $N_0$  is the number of connections of a completely structured material.  
 124 The resulting clay particle model, depicted in Figure 4, can be written as,

$$\begin{aligned}\tau_d + \tau_{s_1} + \tau_{s_2} + \cdots + \tau_{s_N} &= \tau \Rightarrow \\ \tau_d + \gamma_r G_1 + \gamma_r G_2 + \cdots + \gamma_r G_N &= \tau \Rightarrow \\ \tau_d + \gamma_r \frac{NG_0}{N_0} = \tau_d + G_0 \gamma_r \lambda &= \tau,\end{aligned}$$

125 where, the stresses,  $\tau$ 's, are defined in Figure 4, and  $\lambda = \frac{N}{N_0} = \sum_{i=1}^N \frac{G_i}{G_0}$ , is the structure parameter  
 126 with range  $[0, 1]$ . Furthermore,  $\tau_d = \mu \dot{\gamma}$ , where  $\mu$  is the viscosity of the material at  $\lambda = 0$ , and  $\dot{\gamma}$   
 127 is the strain rate tensor. Therefore, the resulting constitutive model is,

$$\tau = \mu \dot{\gamma} + \gamma_r \frac{NG_0}{N_0} = \tau_d + G_0 \gamma_r \lambda. \quad (1)$$

## 128 2.2. Structure Model

129 Experiments have shown that stress and strain controlled measurements performed on clay-  
 130 water suspensions result in different flow curves. In their work on lubricating greases Mas et  
 131 al. [40] observed that the flow curves obtained from strain controlled tests showed a minimum  
 132 stress. The same flow curves obtained using stress controlled tests however, did not show such a  
 133 minimum. Nonetheless, the failure which occurs within the structure of clay-water suspensions  
 134 when yielding is the same for the two types of test. This signifies that the structure parameter  
 135 cannot be a function of only stress or only strain but rather a combination of both that is inde-  
 136 pendent of the type of test that is performed. In this respect energy is a viable choice. Therefore,  
 137 following the work of Moore [14] and Yziquel et al. [27] the time rate of change of the structure  
 138 parameter is written as,

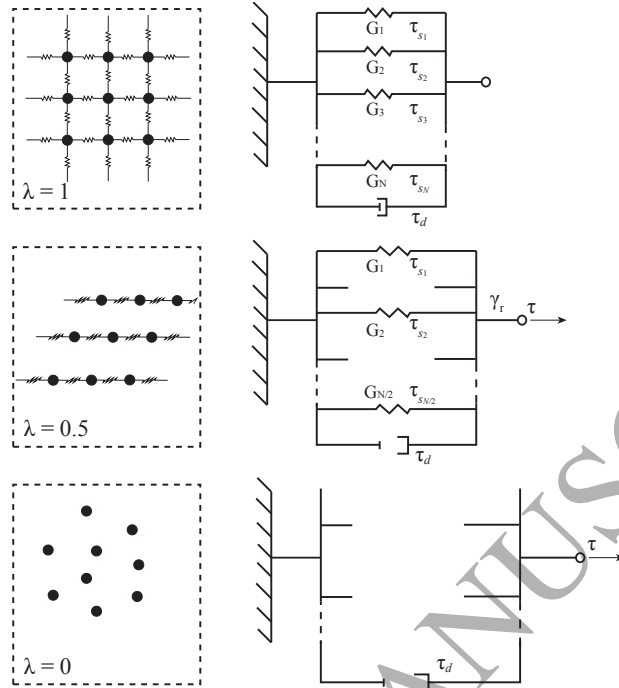


Figure 4: The simplified clay particle network model with complete structure ( $\lambda = 1$ ), top, with half the structure ( $\lambda = 0.5$ ), middle, and with no structure ( $\lambda = 0$ ), bottom.

$$\frac{d\lambda}{dt} = \alpha(1 - \lambda) - |\tau : \dot{\gamma}| \beta \lambda. \quad (2)$$

139 The first term on the right hand side of (2) represents generation of structure by the Brownian  
 140 motion. The second term,  $|\tau : \dot{\gamma}|$ , captures the change in the internal energy of a fluid volume  
 141 due to the application of a stress or strain rate [41]. Once a stress or a strain rate is applied to the  
 142 suspension, it damages the structure (i.e., breaks some connections). This damage can also be  
 143 seen in the increase in the internal energy of the system. Therefore, the increase in the internal  
 144 energy is used to indicate destruction of structure. Note that equation (2) is symmetric with  
 145 respect to  $\dot{\gamma}$  and  $\tau$ . In (2),  $\alpha$  and  $\beta$  are empirical parameters which should be determined through  
 146 experiments.

### 147 2.3. Residual Strain Model

148 Let  $\sum_{i=1}^N \tilde{\gamma}_i(t) \tilde{G}_i$  represent the force applied to a clay particle network with  $N$  number of  
 149 connections at a given time  $t$ . Following the dynamics of the system undergoing a deformation  
 150 with a strain rate  $\dot{\gamma}$ , at a later time  $t + \Delta t$ , let us assume that  $M$  number of connections remain,  
 151  $D$  number of connections are destroyed, and  $C$  number of connections are newly created. The  
 152 strain of the remaining,  $N - D = M$ , connections at  $t + \Delta t$  can be written as,

$$\gamma(t + \Delta t) \approx \dot{\gamma} \Delta t + \tilde{\gamma}(t),$$

153 which results in the following expression for the force applied to the clay particle network at time  
154  $t + \Delta t$ ,

$$\sum_{i=1}^M (\dot{\gamma} \Delta t + \tilde{\gamma}_i(t)) \tilde{G}_i + \sum_{i=1}^C \gamma_i G_i, \quad (3)$$

155 where,  $\gamma_i$  and  $G_i$  are the strains and stiffnesses of the newly created connections, respectively.  
156 Furthermore, from the definition of the residual strain one has,

$$\sum_{i=1}^N \tilde{\gamma}_i(t) \tilde{G}_i = \gamma_r(t) \sum_{i=1}^N \tilde{G}_i = \gamma_r(t) \frac{N}{N_0} G_0 \Rightarrow \gamma_r(t) = \frac{\sum_{i=1}^N \tilde{\gamma}_i(t) \tilde{G}_i}{\frac{N}{N_0} G_0}. \quad (4)$$

157 Similarly, from (3), for the residual strain  $\gamma_r(t + \Delta t)$  one has,

$$\begin{aligned} \sum_{i=1}^M (\dot{\gamma} \Delta t + \tilde{\gamma}_i(t)) \tilde{G}_i + \sum_{i=1}^C \gamma_i G_i &= \gamma_r(t + \Delta t) \sum_{i=1}^{M+C} \tilde{G}_i = \gamma_r(t + \Delta t) \frac{M+C}{N_0} G_0 \Rightarrow \\ \gamma_r(t + \Delta t) &= \frac{\sum_{i=1}^M (\dot{\gamma} \Delta t + \tilde{\gamma}_i(t)) \tilde{G}_i + \sum_{i=1}^C \gamma_i G_i}{\frac{M+C}{N_0} G_0}. \end{aligned} \quad (5)$$

158 Subtracting (4) from (5) and dividing by  $\Delta t$  yields,

$$\begin{aligned} \frac{\gamma_r(t + \Delta t) - \gamma_r(t)}{\Delta t} &= \frac{\sum_{i=1}^M (\dot{\gamma} \Delta t + \tilde{\gamma}_i(t)) \tilde{G}_i + \sum_{i=1}^C \gamma_i G_i}{\frac{M+C}{N_0} G_0 \Delta t} - \frac{\sum_{i=1}^N \tilde{\gamma}_i(t) \tilde{G}_i}{\frac{N}{N_0} G_0 \Delta t} \Rightarrow \dots \\ \dots &= \left( \frac{N_0}{M+C} \right) \sum_{i=1}^M \frac{\dot{\gamma} \tilde{G}_i}{G_0} + \left( \frac{N_0}{M+C} \right) \sum_{i=1}^C \frac{\dot{\gamma} G_i}{G_0} + \left( \frac{M}{M+C} - 1 \right) \frac{\gamma_r(t)}{\Delta t} \Rightarrow \dots \\ \frac{\gamma_r(t + \Delta t) - \gamma_r(t)}{\Delta t} &= \dot{\gamma} - \left( \frac{C}{M+C} \right) \frac{\gamma_r(t)}{\Delta t}. \end{aligned} \quad (6)$$

159 Using the structure model (2) in equation (6),  $C = N_0 \Delta t \alpha (1 - \lambda(t))$  and  $M+C = N_0 \lambda(t + \Delta t)$ ,  
160 which for  $\Delta t \rightarrow 0$ , yields,

$$\frac{d\gamma_r}{dt} = \dot{\gamma} - \frac{\alpha(1-\lambda)}{\lambda} \gamma_r. \quad (7)$$

161 Note that in the derivation of expression (6) no assumption was made regarding the regime  
162 of the flow, therefore, this expression holds for laminar as well as turbulent flows.

163 Combining (1), (2), and (7), results in the following rheological model,

$$\tau = G_0 \lambda \gamma_r + \mu \dot{\gamma}, \quad (8)$$

$$\dot{\lambda} = \alpha(1-\lambda) - |\tau : \dot{\gamma}| \beta \lambda, \quad (9)$$

$$\dot{\gamma}_r = \dot{\gamma} - \frac{\alpha(1-\lambda)}{\lambda} \gamma_r. \quad (10)$$

164 Generalization of (8) to (10) for the case of simple shear and vortex flows in three dimensions  
165 is given in Appendix A and Appendix B.

166 2.4. Evolution of the structure parameter,  $\lambda$ , for various values of stress

167 In equilibrium, the number of connections created equals the number of connections de-  
 168 stroyed, therefore,  $\dot{\lambda} = 0 \Rightarrow \lambda_e = \alpha / (\alpha + \beta|\tau : \dot{\gamma}|)$  and the rate of change of residual strain is  
 169 zero, i.e.,  $\dot{\gamma}_r = 0$ . Therefore,

$$\frac{d\gamma_r}{dt} = \dot{\gamma} - \frac{\gamma_r \alpha (1 - \lambda_e)}{\lambda_e} = 0 \Rightarrow \gamma_r = \frac{\lambda_e \dot{\gamma}}{\alpha (1 - \lambda_e)}. \quad (11)$$

170 Inserting (11) in (8) yields the effective viscosity,

$$\tau = \left( \frac{G_0 \lambda_e^2}{\alpha (1 - \lambda_e)} + \mu \right) \dot{\gamma} \Rightarrow \mu_e(\lambda_e) = \frac{G_0 \lambda_e^2}{\alpha (1 - \lambda_e)} + \mu. \quad (12)$$

171 Hence,

$$\dot{\gamma} = \frac{\tau \alpha (1 - \lambda_e)}{G_0 \lambda_e^2 + \mu \alpha (1 - \lambda_e)}. \quad (13)$$

172 Inserting (13) in (9) yields,

$$\frac{d\lambda}{dt} = \alpha (1 - \lambda_e) - \frac{\tau^2 \alpha (1 - \lambda_e)}{G_0 \lambda_e^2 + \mu \alpha (1 - \lambda_e)} \beta \lambda_e = 0, \quad (14)$$

173 which results in,

$$\alpha (1 - \lambda_e) \left[ 1 - \frac{\tau^2 \beta \lambda_e}{G_0 \lambda_e^2 + \mu \alpha (1 - \lambda_e)} \right] = 0. \quad (15)$$

174 The roots to (15) are,

$$\lambda_{e,y} = 1, \text{ and,} \quad (16)$$

$$\lambda_{e,\pm} = \frac{\mu \alpha + \beta \tau^2 \pm \sqrt{(\mu \alpha + \beta \tau^2)^2 - 4 G_0 \mu \alpha}}{2 G_0}. \quad (17)$$

175 Only one solution to (17) exists when,  $|\tau| = \sqrt{(\sqrt{4 G_0 \mu \alpha} - \mu \alpha) / \beta}$ . This shear stress is called  
 176 the critical stress,  $\tau_c$ , and is the stress below which a flowing material comes to a stop.

177 At yield stress  $\tau = \tau_y$ , two solutions exist for (17), however, one of them coincides with (16).

178 Inserting  $\lambda_{e,y} = 1$  in (17) yields,  $|\tau_y| = \sqrt{G_0 / \beta}$ . The other root,  $\lambda_{e,-}$ , can be obtained by inserting  
 179  $\tau_y$  back into equation (17). This yields,  $\lambda_{e,-} = \mu \alpha / G_0$ . Once  $\tau = \tau_y$ ,  $\lambda_{e,-}$  is the stable solution  
 180 where the structure will end up (since  $\lambda_{e,y} = 1$  becomes unstable at this point and the material  
 181 begins to flow).

182 Figure 5 depicts the development of the structure parameter,  $\lambda$ , for various initial structures,  $\lambda_0$ ,  
 183 under different constant stresses.

184 For stresses  $\tau_c < \tau < \tau_y$ , if the material is flowing, it will end up with a structure  $\lambda_e = \lambda_{e,-} < 1$ .

185 However, if the material has not disintegrated, i.e.,  $\lambda_e < \lambda_{e,+}$ , then it will end up at  $\lambda_{e,y} = 1$ .

186

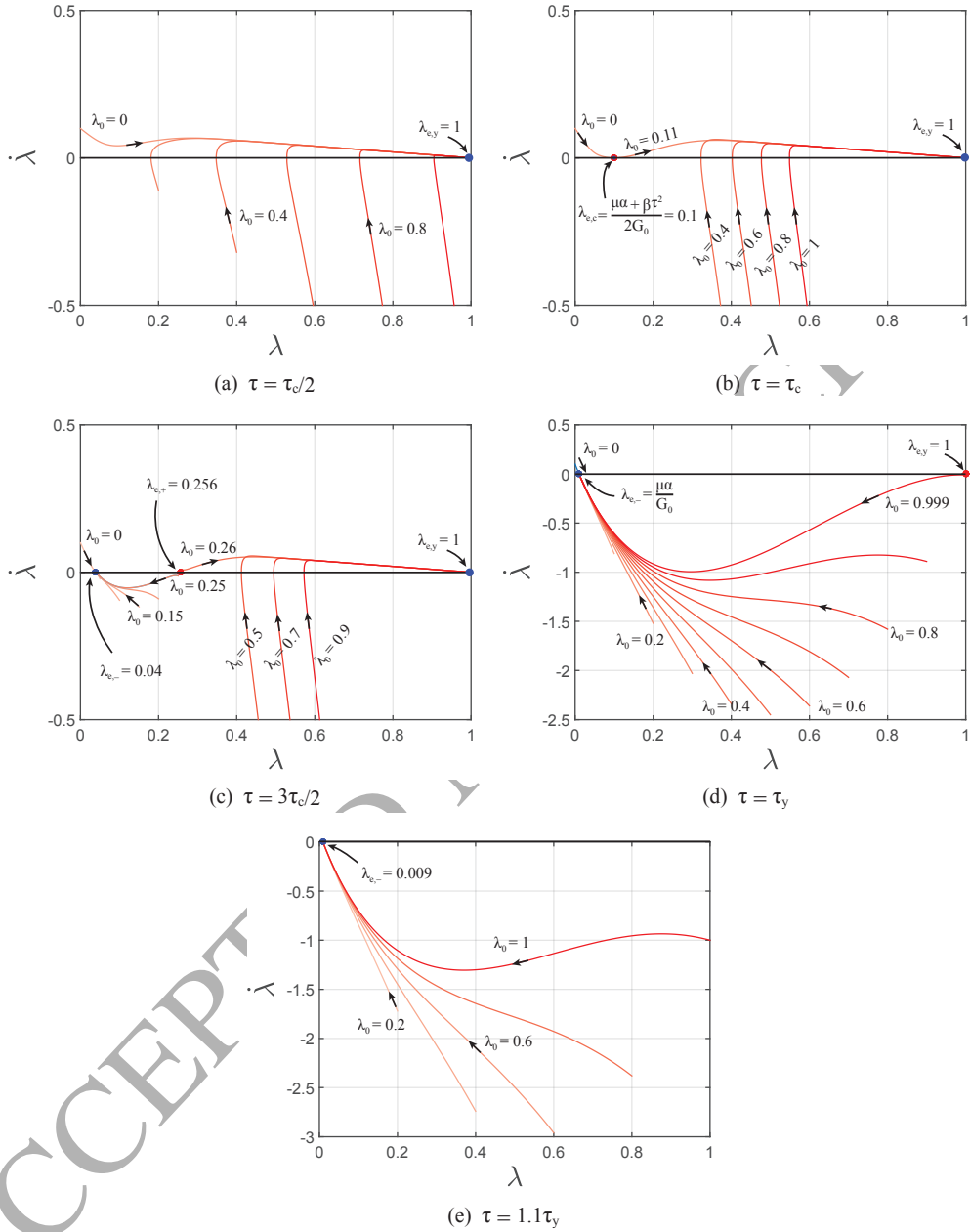


Figure 5: Change in the structure parameter,  $\lambda$ , with time, for various initial structures,  $\lambda_0$ , under different stress conditions.

187 2.5. Evolution of the structure parameter,  $\lambda$ , for various values of strain rate

188 Following the same procedure as in section 2.4, and writing the stress in terms of the strain  
 189 rate, equation (15) becomes,

$$(\beta G_0 \dot{\gamma}^2) \lambda_e^3 - (\mu \dot{\gamma}^2 \beta \alpha + \alpha^2) \lambda_e^2 + (\mu \dot{\gamma}^2 \beta \alpha + 2\alpha^2) \lambda_e - \alpha^2 = 0. \quad (18)$$

190 For all the empirical parameters considered in this study (and perhaps for all appropriate values  
191 of  $\beta$ ,  $G_0$ ,  $\dot{\gamma}$ ,  $\mu$ , and  $\alpha$ ) this equation only has one real solution.

192 Let  $b = -\frac{\mu \dot{\gamma}^2 \beta \alpha + \alpha^2}{\beta G_0 \dot{\gamma}^2}$ ,  $c = \frac{\mu \dot{\gamma}^2 \beta \alpha + 2\alpha^2}{\beta G_0 \dot{\gamma}^2}$ ,  $d = \frac{-\alpha^2}{\beta G_0 \dot{\gamma}^2}$ ,  $p = c - \frac{1}{3}b^2$ , and  $q = d - \frac{1}{3}bc + \frac{2}{27}b^3$ . Then for  $p > 0$   
193 the real solution to (18) can be written as [42],

$$\lambda_e = -b/3 - 2\sqrt{p/3} \sinh\left(\frac{1}{3} \operatorname{arcsinh}\left(\frac{q/2}{(p/3)^{3/2}}\right)\right). \quad (19)$$

194 For an imposed strain rate, if  $\lambda < \lambda_e$ , then the structure parameter,  $\lambda$ , grows in time to reach  
195  $\lambda_e$ . If on the other hand  $\lambda > \lambda_e$ , then the structure parameter decreases in time to reach  $\lambda_e$ . Figure  
196 6 depicts the development of the structure parameter,  $\lambda$ , for various initial structures,  $\lambda_0$ , under a  
197 constant strain rate.

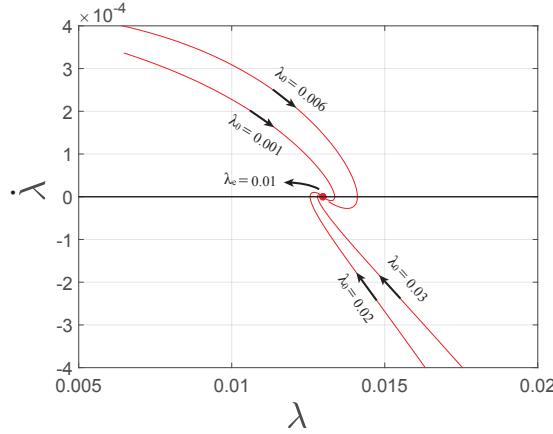


Figure 6: Change in the structure parameter,  $\lambda$ , with time, for various initial structures,  $\lambda_0$ , under a constant strain rates.

## 198 2.6. Solutions at constant values of $\dot{\gamma}$ and $|\tau : \dot{\gamma}|$

199 For constant values of  $|\tau : \dot{\gamma}|$  in time, (9) can be solved to obtain,

$$\lambda = (\lambda_0 - \lambda_e) e^{-(\alpha + \beta|\tau : \dot{\gamma}|)t} + \lambda_e, \quad (20)$$

200 where,  $\lambda_0 = \lambda(t = 0)$ .

201 A more complex relation can be derived for the residual strain for constant values of  $\dot{\gamma}$  and  $|\tau : \dot{\gamma}|$ ,

$$\gamma_r = \frac{1}{u} \int \dot{\gamma} u dt + C, \quad (21)$$

202 where,  $C$  is a constant and,

$$u = \left(\frac{\lambda_0 - \lambda_e}{\lambda_e} + e^{(\alpha + \beta|\tau : \dot{\gamma}|)t}\right)^{1 - \lambda_e} + \left(\frac{\lambda_0 - \lambda_e}{\lambda_e} + e^{-(\alpha + \beta|\tau : \dot{\gamma}|)t}\right)^{\lambda_e}. \quad (22)$$

203 The complications in solving the integral in (21) can be avoided by introducing a new variable  
 204  $\zeta = \lambda\gamma_r$ . The rheological model then reads,

$$\tau = G_0\zeta + \mu\dot{\gamma}, \quad (23)$$

$$\dot{\lambda} = \alpha(1 - \lambda) - |\tau : \dot{\gamma}|\beta\lambda, \quad (24)$$

$$\dot{\zeta} = \dot{\gamma}\lambda - |\tau : \dot{\gamma}|\beta\zeta. \quad (25)$$

205 For constant values of  $\dot{\gamma}$  and  $|\tau : \dot{\gamma}|$ , equation (25) can be solved to obtain,

$$\zeta = \frac{\dot{\gamma}(\lambda_e - \lambda_0)}{\alpha} e^{-(\alpha + \beta|\tau : \dot{\gamma}|)t} + \lambda_e \frac{\dot{\gamma}}{\beta|\tau : \dot{\gamma}|} + \left[ (\gamma_{r0} + \frac{\dot{\gamma}}{\alpha})\lambda_0 - (\frac{\dot{\gamma}}{\beta|\tau : \dot{\gamma}|} + \frac{\dot{\gamma}}{\alpha})\lambda_e \right] e^{-\beta|\tau : \dot{\gamma}|t}, \quad (26)$$

206 where,  $\gamma_{r0} = \gamma_r(t = 0)$ .

### 207 2.7. Types of flow curves

208 Let  $f$  be a map sending  $\lambda_e$  to its corresponding stress  $\tau$ , i.e.,  $f(\lambda_e) : \lambda_e \rightarrow \tau$ , and let  $g$  be  
 209 a map sending  $\lambda_e$  to its corresponding strain rate,  $\dot{\gamma}$ , i.e.,  $g(\lambda_e) : \lambda_e \rightarrow \dot{\gamma}$ . Then following the  
 210 discussion in Sections 2.4 and 2.5,  $f$  is non-injective, while  $g$  is bijective.

211 Let us imagine a material with a complete structure,  $\lambda = 1$ , and increase the stress until  $\tau = \tau_y$ .  
 212 Increasing  $\tau$  beyond  $\tau_y$  results in a jump in the equilibrium structure parameter from  $\lambda = 1$  to  
 213  $\lambda_{e,-}$ . Since  $g$  is bijective, the strain rate also shows a jump at this point from  $g(\lambda = 1) = \dot{\gamma}_{e,y}$  to  
 214  $g(\lambda_{e,-}) = \dot{\gamma}_{e,-}$ . This path is shown in Figure 7 by red arrows.

215 Now imagine a material under a high shear stress and with zero structure,  $\lambda = 0$ , and decrease  
 216 the stress until  $\tau = \tau_c$ . Decreasing  $\tau$  beyond  $\tau_c$  results in a jump in the equilibrium structure  
 217 parameter from  $\lambda_{e,c}$  to  $\lambda = 1$ . Again, since  $g$  is bijective, the strain rate also shows a jump at this  
 218 point from  $g(\lambda_{e,c}) = \dot{\gamma}_c$  to  $g(\lambda = 1) = \dot{\gamma}_{e,y}$ . This path is shown in Figure 7, by black arrows.

219 Note that in Figure 7, the slope of the initial rise in the flow curve, resembling elastic solid  
 220 behavior, as well as the stress at the point of yielding, are dependent on the speed at which the  
 221 stress is increased. This topic will be explained more thoroughly in section 2.8.

222 Non-injectivity of  $f$ , results in a different picture for strain controlled hysteresis plots. For  
 223  $\tau_c < \tau < \tau_y$ , there are three equilibrium structure parameters (non-injectivity of  $f$ ) and each  
 224 structure parameter corresponds to only one shear rate (bijectivity of  $g$ ). Consequently, multi-  
 225 ple strain rate values correspond to one specific stress in this regime. Figure 8 shows a strain  
 226 controlled hysteresis plot. The red and black arrows show the path of increasing and decreasing  
 227 strain rate, respectively.

228 Note that the model has the ability to capture the critical yield stress, i.e., the minimum stress in  
 229 a strain controlled flow curve. For clay-water suspensions, the falling region of the flow curve  
 230 corresponds to the shear banding instability [9]. The model has an unstable equilibrium solution  
 231 in this transitional region and therefore, mimics the physical behavior of the material well in this  
 232 regime.

233 For  $\tau_y = 0$  or  $\dot{\gamma} \rightarrow \infty$ , the model presented in (23) simplifies to the Newtonian fluid model,  
 234  $\tau = \mu\dot{\gamma}$ . Furthermore, for  $\alpha \rightarrow \infty$ ,  $\tau_c \rightarrow \tau_y$ , and (23) resembles the Bingham elastic model [43].

235 For all the other cases, the rheological model presented by equations (23) to (25) describes a  
 236 thixotropic yield stress fluid.

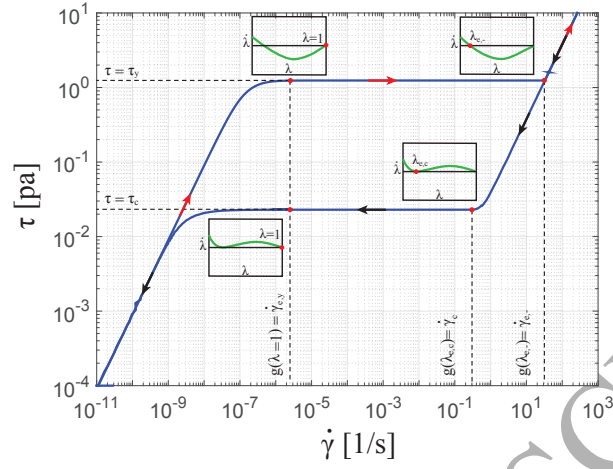


Figure 7: Stress controlled hysteresis plot obtained from equations (23) to (25). The red arrows show the path of increasing stress and the black arrows show the path of decreasing stress. The inset plots depict the bifurcation of the structure parameter.

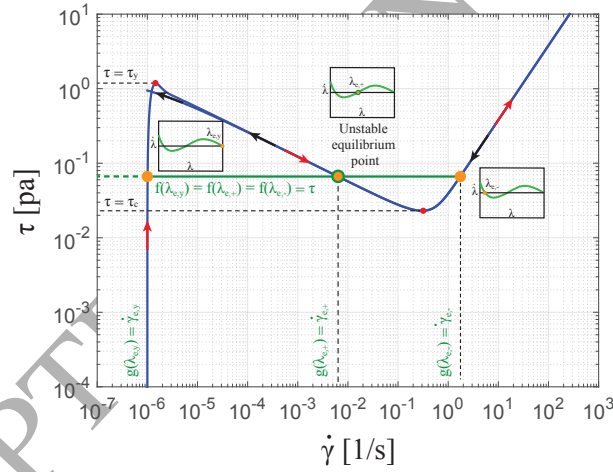


Figure 8: Strain controlled hysteresis plot obtained from equations (23) to (25). The red arrows show the path of increasing strain rate and the black arrows show the path of decreasing strain rate. The inset plots depict the bifurcation of the structure parameter.

## 237 2.8. Apparent yield stress

238 In order to make a stationary material with a structure parameter,  $\lambda < 1$ , flow, one has to  
 239 overcome the apparent yield stress that corresponds to  $\lambda_{e,+}$  (Figure 5), i.e.,

$$|\tau_{y,+}| = \sqrt{\frac{G_0 \lambda_{e,+}^2 + \mu \alpha (1 - \lambda_{e,+})}{\beta \lambda_{e,+}}}. \quad (27)$$

240 In general, the structure state of a stationary material at a given time is  $\lambda_{e,+}$ . Therefore, in order  
 241 to break this structure, a stress level higher than  $|\tau_{y,+}|$ , where,  $\tau_c < \tau_{y,+} < \tau_y$ , should be imposed  
 242 on the material. For  $\lambda_{e,+} = 1$ ,  $\tau_{y,+} = \tau_y$ , and for  $\lambda_{e,+} = \lambda_{e,c}$ ,  $\tau_{y,+} = \tau_c$  (Figure 5). Once  $\tau_y < \tau$ ,  
 243 there are no longer any unstable equilibrium structure points,  $\lambda_{e,+}$ , and consequently, there are  
 244 no apparent yield stresses.

245 In stress versus strain rate plots, the apparent yield stress is the stress at which the jump in strain  
 246 rate occurs. To analyze such a case, let  $\tau = \tau(t)$ , be a logarithmic staircase function with a  
 247 constant step duration,  $\Delta t$ , (inset plot of Figure 9(a)). During each step duration,  $\Delta t$ , equations  
 248 (23) to (25) are then solved for each constant stress. Figure 9(a) shows the stress versus the strain  
 249 rate value that is obtained at the end of each time step. Figure 9(b) shows the stress versus the  
 250 structure parameter in blue and the apparent yield stress,  $\tau_{y,+}$ , versus  $\lambda_{e,+}$  in red, all computed at  
 251 the end of each time step. The point where the blue and the red curves cross corresponds to the  
 252 structure state at which  $\tau_{y,+} < \tau$ , and the material first begins to flow, i.e.,  $\lambda \rightarrow \lambda_{e,-}$  (Figure 5).

Since from the apparent/transient stress versus strain rate plots (experimental or in this case

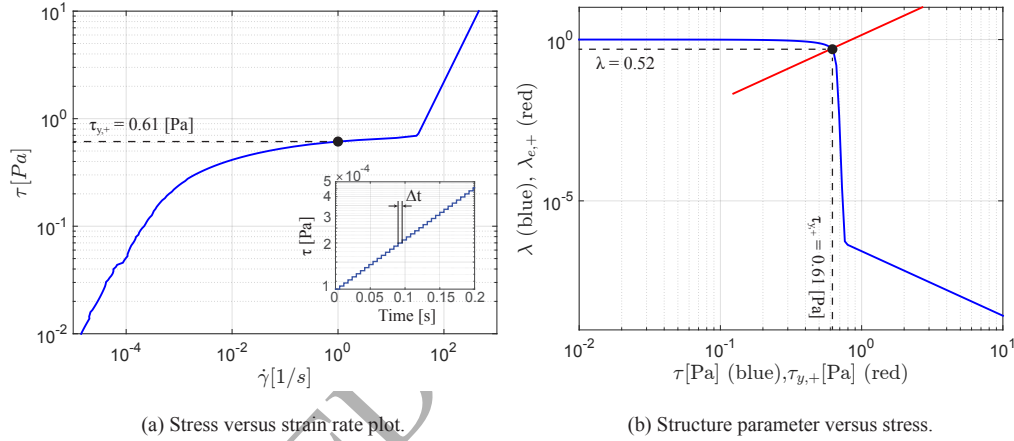


Figure 9: Transient stress versus strain rate plot (a), and structure parameter versus stress curve (b), obtained at the end of each time interval  $\Delta t$ , for a logarithmic staircase input function shown in the inset plot of (a). The red and blue curves in (b) show the change in  $\lambda_{e,+}$  with the apparent yield stress  $\tau_{y,+}$ , and the structure parameter,  $\lambda$ , with stress,  $\tau$ , respectively.

253 numerical), one can only obtain the apparent yield stress,  $\tau_{y,+}$ , reverse engineering must be done  
 254 to obtain the value of  $\tau_y$ .  
 255

## 256 2.9. Relation to other models

257 The rheological model presented in this study is analogous to those from the studies of Mu-  
 258 jumdar et al. [33] and Dullaert and Mewis [34]. The fundamental difference between these  
 259 models is with regards to their formulations of the elastic strain and the structure parameter. Al-  
 260 though, a complete evaluation of the dis/similarities between these models is outside the scope  
 261 of the current work, in this section some of these points are briefly discussed. Table 1 lists the  
 262 three rheological models.  
 263

264

Authors	Const. model	Structure model	Elastic strain model	Emp. parameters
Mujumdar et al. [33]	$\tau = \lambda G \gamma_e + (1 - \lambda) K \dot{\gamma}^n$	$\dot{\lambda} = k_1 \dot{\gamma}_+ \lambda + k_2 (1 - \lambda), \dot{\gamma}_+ = \begin{cases} 0 & : \dot{\gamma} \gamma_e \leq 0, \\ 0 & : \dot{\gamma} \gamma_e > 0. \end{cases}$	$\begin{cases} \dot{\gamma}_e = \dot{\gamma} :  \gamma_e  < \gamma_{co} \lambda^m, \\ \dot{\gamma}_e = \gamma_{co} \lambda^m :  \gamma_e  > \gamma_{co} \lambda^m. \end{cases}$	$G, n, K, k_1, k_2, \gamma_{co}, m$
Dullaert and Mewis [34]	$\tau = \lambda G_0 \gamma_e + \lambda \eta_{st,0} \dot{\gamma} + \eta_{\infty} \dot{\gamma}$	$\dot{\lambda} = (1/t^\beta) (-k_1 \dot{\gamma} \lambda + k_2 \dot{\gamma}^{0.5} (1 - \lambda) + k_3 (1 - \lambda))$	$\dot{\gamma}_e = (1/t)^\beta (\tau \gamma_e - \tau_{ss} \dot{\gamma}_e)$	$\gamma_c, G_0, \eta_{st,0}, \eta_{\infty}, \beta, k_1, k_2, k_3$
This Study	$\tau = \lambda G_0 \gamma_r + \mu \dot{\gamma}$	$\dot{\lambda} = -\beta \tau : \dot{\gamma} \lambda + \alpha (1 - \lambda)$	$\dot{\gamma}_r = \dot{\gamma} - \frac{\gamma_e \alpha (1 - \lambda)}{\lambda}$	$\mu, G_0, \alpha, \beta$

Table 1: The structural kinetic models of Mujumdar et al. [33], Dullaert and Mewis [34], and this study.

### 2.9.1. Comparison to the model of Mujumdar et al. [33]

In [33], Mujumdar et al. present a model based on the network association theory where the material is viewed as a network of small indivisible particles. Once shear is applied to the material, the network breaks down into flocs. If breakdown is continued, the flocs eventually decompose into individual particles. In their formulation, the time-dependent elastic limit of the material is related to the size of the flocs via the structure parameter and an exponent,  $m$ , that characterizes the elastic limit of the flocs.

It is difficult to express the phenomenology that is presented in [33] (regarding the breakdown of the network into flocs and ultimately into particles) with a picture, such as the one shown in Figure 4. Similar to [33], the model that is presented in the current study is based on the network theory. However, unlike the model of Mujumdar et al., here it is assumed that the behavior of the material is uniform and scale invariant. This precludes the need for an exponent such as  $m$ .

A key feature of the model of Mujumdar et al. is a smooth transition from an elastically dominated response to a viscous response, with no discontinuity in the stress-strain curve (Figure 10(b)). Nonetheless, the formulation of both the structure parameter and the elastic strain are discontinuous in their work, which makes numerical computation cumbersome (Table 1).

Analogous to [33], the model presented here allows for a smooth transition from an elastically dominated response to a viscous response, with no discontinuity in the stress-strain curve (Figure 10(a)). However, in contrast to [33], the formulations of both, the structure parameter and the elastic strain, are continuous in the model presented here.

Following the same procedure as in section 2.4, the evolution of the structure parameter under various stress conditions can be evaluated for the model in [33]. To allow comparison with the current study, let the parameter  $n = 1$  (no shear thinning) in Table 1. Then, in equilibrium, the following expression can be derived for the structure parameter,

$$k_1 G \gamma_{co} \lambda_e^{m+1} + K k_2 \lambda_e^2 - 2K k_2 \lambda_e + K k_2 - k_1 \tau = 0. \quad (28)$$

It can be seen that depending on the value of the exponent,  $m$ , equation (28) can have different numbers of roots. For instance for  $m = -0.3$  (a representative case from [33]), this equation has in total 20 roots, repeated, as well as distinct (this can be shown by a change of variable from  $\lambda_e$  to  $Q$ , where  $Q^{10} = \lambda_e$ ). This suggests that the model of Mujumdar et al. may be difficult to interpret with regards to the phenomenon of viscosity bifurcation.

Figure 11 shows the strain controlled flow curves obtained from the model of Mujumdar et al. [33] (blue), and from the current study (red). It can be seen that qualitatively, the two models result in very similar flow curves. Nonetheless, there are small discrepancies that make the differences between the two models more conspicuous. A  $C^1$  discontinuity can be observed within the non-linear elastic regime of the blue curve. This is not the case for the flow curve obtained from the current study. Furthermore, the two models show slightly different behavior at the end of the liquefaction and the beginning of the viscous regimes.

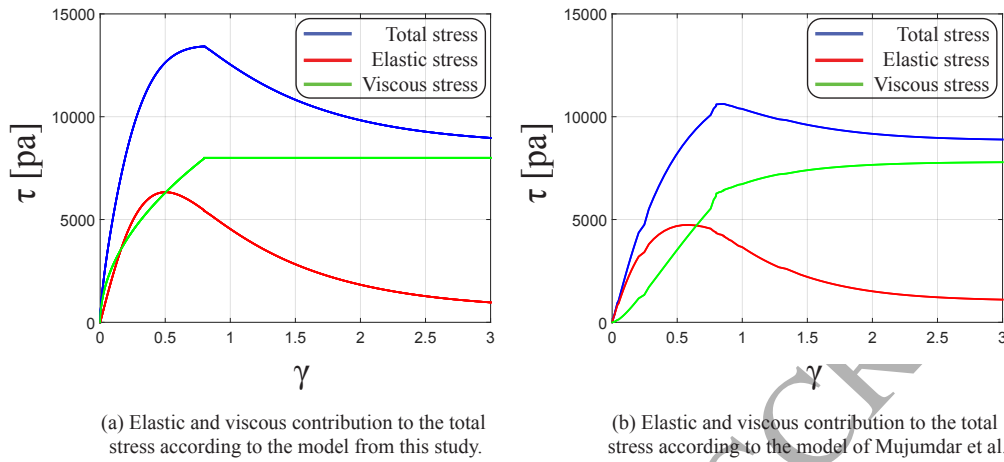


Figure 10: Prediction of the elastic, viscous, and total stress response from the model presented in the current study (a), and from the model presented by Mujumdar et al. [33] (b), during the start-up of a steady shear flow,  $\dot{\gamma} = 20 \text{ s}^{-1}$ . The parameters used in the model from this study are:  $G_0 = 25000 \text{ Pa}$ ,  $\alpha = 1 \text{ s}^{-1}$ ,  $\mu = 400 \text{ Pa} \cdot \text{s}$ ,  $\beta = 0.00016 \text{ Pa}^{-1}$ . The parameters used in the model of Mujumdar et al. are:  $G = 25000 \text{ Pa}$ ,  $K = 400 \text{ Pa} \cdot \text{s}$ ,  $k_1 = 2$ ,  $k_2 = 1 \text{ s}^{-1}$ ,  $\gamma_{co} = 0.5$ ,  $n = 1$ ,  $m = -0.33$ .

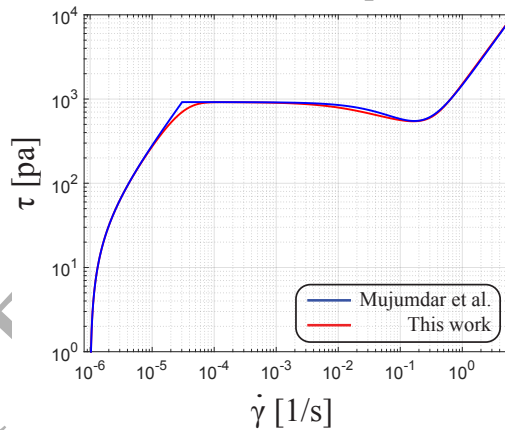


Figure 11: Strain controlled flow curves obtained from the model of Mujumdar et al. [33] (blue), and from the current study (red). The parameters used to obtain the blue curve are:  $G = 40000 \text{ Pa}$ ,  $K = 1500 \text{ Pa} \cdot \text{s}$ ,  $k_1 = 10$ ,  $k_2 = 1 \text{ s}^{-1}$ ,  $\gamma_{co} = 0.023$ ,  $n = 1$ ,  $m = 0.15$ . The parameters used to obtain the red curve are:  $G_0 = 40000 \text{ Pa}$ ,  $\alpha = 1 \text{ s}^{-1}$ ,  $\mu = 1500 \text{ Pa} \cdot \text{s}$ ,  $\beta = 0.04 \text{ Pa}^{-1}$ .

301 Finally, the model presented by Mujumdar et al. contains six empirical parameters (not including  
302  $n$ ). In contrast, the model presented in this study has four parameters.

### 303 2.9.2. Comparison to the model of Dullaert and Mewis [34]

304 In [34], Dullaert and Mewis present a general structural kinetic model to describe the flow  
305 behavior of thixotropic systems. Analogous to the current study, in their work the total stress is  
306 divided into a structure-dependent elastic and a viscous contribution.

307 To describe the elastic contribution, Dullaert and Mewis propose a single stress-dependent ki-  
 308 netic equation that allows the aggregates to relax after a reduction in hydrodynamic stress and  
 309 stretch when the stress is increased. This is in contrast to the approach taken in the current study  
 310 where, the kinetic equation for the elastic strain of the flowing structure is derived from the first  
 311 principles using the structure model, and based on a set of physical assumptions regarding parti-  
 312 cle interactions at the micro-scale.

313 Dullaert and Mewis state that the model in [34] can predict overshoot stresses that are larger than  
 314 the apparent yield stress during start up flows. The model presented herein however, does not  
 315 predict such overshoot stresses. According to the model in the current study, as soon as shear  
 316 is applied to the material, the structure begins to break down. Depending on the strain rate, the  
 317 structure can break down faster (higher strain rates), or slower (lower strain rates), which in turn  
 318 can cause the material to reach its yield point quickly, or slowly. The stress at the point of yield-  
 319 ing is here referred to as the apparent yield stress and is always smaller than the true yield stress  
 320 of the material. During start up flows, the stress can quickly reach the apparent yield stress (stress  
 321 over-shoot) and subsequently drop to the stress of the flowing material (Section 4.2). However,  
 322 it can never exceed the apparent yield stress of the material.

323 According to Dullaert and Mewis, upon cessation of flow, the model in [34] can predict non-zero  
 324 values for the stress. The model presented in this study also has this attribute (Section 4.1). The  
 325 structure model in [34] is not symmetric with respect to the stress and the strain rate. The struc-  
 326 ture model employed in this study however, is symmetric.

327 Following the same procedure as in section 2.4, the evolution of the structure parameter under  
 328 various stress conditions can be evaluated for the model in [34]. This results in the following  
 329 expression for the structure parameter in equilibrium,

$$-k_1 \left( \frac{\tau - G_0 \lambda_e \gamma_c}{\eta_{st,0} \lambda_e + \eta} \right) \lambda_e + k_2 \left( \frac{\tau - G_0 \lambda_e \gamma_c}{\eta_{st,0} \lambda_e + \eta} \right)^{1/2} (1 - \lambda_e) + k_3 (1 - \lambda_e) = 0. \quad (29)$$

330 The roots of this expression are difficult to obtain. This suggests that the model of Dullaert and  
 331 Mewis may be difficult to interpret with regards to the phenomenon of viscosity bifurcation.

332 Figure 12 shows the strain controlled flow curves obtained from the model of Dullaert and Mewis  
 333 [34] (blue), and from the current study (red). It can be seen that qualitatively, the two models  
 334 result in quite different flow curves. The red curve is non-monotonic and has a minimum. While  
 335 the blue curve is a monotonically increasing flow curve. The two curves predict very different  
 336 material behaviors within the non-linear elastic and the liquefaction regimes. However, some of  
 337 these differences may be attributed to the values of the empirical parameters used here.

338 Finally, the model presented by Dullaert and Mewis contains eight empirical parameters. In  
 339 contrast, the model presented in this study has four parameters.

### 340 3. Methodology for obtaining the empirical parameters and the rheometric validation tests

341 In this section the methodology behind the stress and strain controlled measurements which,  
 342 (1) can be used to obtain the empirical parameters,  $\mu$ ,  $G_0$ ,  $\tau_y$ , and  $\alpha$  (note that  $\beta = G_0/\tau_y^2$ ), and  
 343 (2) are used to evaluate the performance of the model, are explained.

344 The stress controlled shearing conditions within the boundary layer of sediment gravity flows are  
 345 simulated using stress controlled stress versus strain rate curves. The stress controlled shearing  
 346 conditions within the boundary layer eddies are simulated using oscillatory stress controlled am-  
 347 plitude sweep tests. The strain controlled shearing conditions within the free shear and boundary

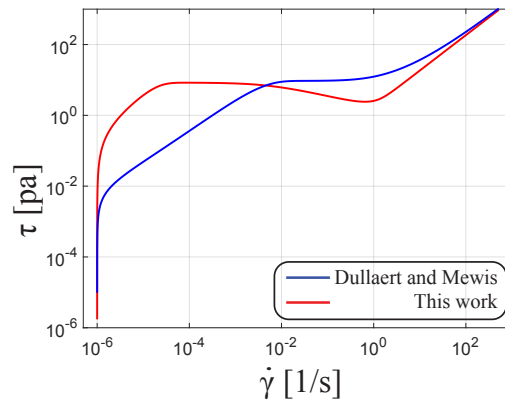


Figure 12: Strain controlled flow curves obtained from the model of Dullaert and Mewis [34] (blue), and from the current study (red). The parameters used to obtain the blue curve are:  $\gamma_c = 0.015$ ,  $G_0 = 560 \text{ Pa}$ ,  $\eta_{st,0} = 8.6 \text{ Pa} \cdot \text{s}$ ,  $\eta_\infty = 1.84 \text{ Pa} \cdot \text{s}$ ,  $\beta = 0.37$ ,  $k_1/k_3 = 0.99 \text{ s}$ ,  $k_2/k_3 = 0.42 \text{ s}^{0.5}$ ,  $k_3 = 0.20 \text{ s}^{\beta-1}$ . The parameters used to obtain the red curve are:  $G_0 = 560 \text{ Pa}$ ,  $\alpha = 0.55 \text{ s}^{-1}$ ,  $\mu = 1.84 \text{ Pa} \cdot \text{s}$ ,  $\beta = 7.9 \text{ Pa}^{-1}$ .

348 layers are simulated using strain controlled stress versus strain rate curves. For the computations,  
 349 equations (23) to (25) are solved numerically using a variable order backward differentiation for-  
 350 mula [44].

351

### 352 3.1. Mixture preparation and measurement considerations and apparatus

353 Mixture of quartz sand from Sibelco with median diameter of  $150 \mu\text{m}$  and Crown Kaolinite  
 354 clay from ActiveMinerals International, with median diameter of  $0.18 \mu\text{m}$  were prepared. The  
 355 sediment volume concentration was varied between 9%, 12.65%, 15%, 17.82%, and 21% and  
 356 contained 2/3 sand and 1/3 clay. For the dilute case of 9% sediment concentration, the suspen-  
 357 sion is close to the gelling concentration and the low stress measurements may be influenced by  
 358 artifacts such as surface tension or the shape of the sample periphery. Therefore, the data for this  
 359 case is not included during apparent yield stress or shear modulus fitting (Figure 14).

360 MRC302 Anton Paar rheometer was used for all the measurements. To reduce the effect of set-  
 361 tling on the measurements, a concentric cylinder geometry was used. The inner cylinder diameter  
 362 was  $28.92 \text{ mm}$ . In order to avoid wall slip a sandblasted bob with a diameter of  $26.663 \text{ mm}$  and a  
 363 surface roughness of  $4\text{--}7 \mu\text{m}$  was used. The mixtures were introduced inside the cylinder with a  
 364 syringe. A cover was used during the tests to reduce water evaporation. The measurements were  
 365 performed at a temperature of  $20^\circ\text{C}$ .

### 366 3.2. Oscillatory stress controlled amplitude sweep tests and shear modulus, $G_0$ , measurements

367 For low values of strain,  $\lambda \approx 1 \Rightarrow N \approx N_0$ , and  $G' \approx G_0$ . Therefore, the value of  $G_0$  can be  
 368 approximated by the value of the storage modulus,  $G'$ , obtained from amplitude sweep tests at  
 369 low values of strain.

370 Prior to the measurements, the samples were left at rest for a period of 3000 seconds in order to  
 371 regain structure. Subsequently, stress controlled amplitude sweep tests were performed on the  
 372 samples. The stress amplitude was increased from  $0.0001 \text{ Pa}$  to various final values depending  
 373 on the sediment concentration, and the angular frequency was set to  $10 \text{ rad/s}$ .

374 Figure 13 depicts the storage,  $G'$ , and loss,  $G''$ , moduli as a function of strain for a representative  
 375 sample with 12.65% sediment concentration. The dashed line represents the value of  $G_0$  approx-  
 376 imated by the value of  $G'$  from the linear part of stress controlled amplitude sweep plots. Similar  
 377 plots were obtained for other sediment concentrations.

378 Figure 14(a) depicts the shear modulus,  $G_0$ , obtained for various sediment concentration after a  
 379 rest period of 3000 seconds. The dashed line in Figure 14(a) was obtained by fitting a power law  
 380 function to the measurement data. The data for the 9% sediment concentration was not consid-  
 381 ered during fitting (section 3.1). The resulting  $R^2$  goodness of fit value of this power law function  
 382 is 0.99.

383

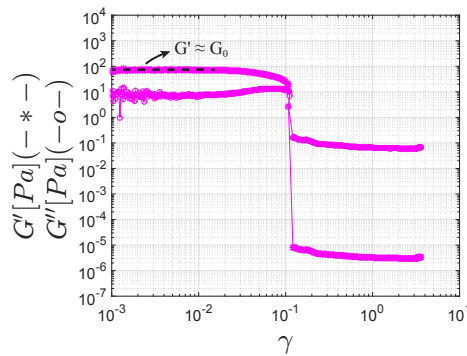


Figure 13: Storage and loss moduli versus strain obtained from stress controlled amplitude sweep test for a sample with 12.65% sediment concentration, after a resting period of 3000 seconds. The dashed line represents the approximated value of elastic modulus,  $G_0$ .

### 384 3.3. Yield stress, $\tau_y$ , and viscosity, $\mu$ , measurements

385 The yield stress and the viscosity values of the mixtures can be obtained from stress controlled  
 386 rheometry tests. Prior to the measurements, the mixtures were poured into the cylinder  
 387 geometry and were left to rest for 3000 seconds in order to regain structure. Stress was then  
 388 increased from 0.0001 Pa to 1.6, 8, 11, 20, and 25 Pa for 9%, 12.65%, 15%, 17.82%, and 21%  
 389 sediment concentrations, respectively. The duration for obtaining a data point was set to 2 sec-  
 390 onds.

391 Figure 15 depicts the measurement result of a representative sample with 12.65% concentration  
 392 for  $0.01 < \dot{\gamma}$ . The value of the apparent yield stress,  $\tau_{y,+}$ , and viscosity,  $\mu$ , were obtained from the  
 393 plots (Figure 15). Equations (23) to (25) were then solved for the same input stress parameters  
 394 as for the measurements. Assuming 3000 seconds was enough time to reach complete structure  
 395 ( $\lambda = 1$ ), the initial conditions were set to  $\lambda_0 = 1$  and  $\gamma_{r0} = 0$ . The value of  $\tau_y$  for each concen-  
 396 tration was then adjusted such that the value of  $\tau_{y,+}$  obtained from the model matched its value  
 397 from the measurements.

398 Figure 14 shows the values of the viscosity and the apparent yield stress for different sediment  
 399 concentrations. Curve fitting was then performed on the results. The apparent yield stress data  
 400 for the 9% sediment concentration was not considered during fitting (section 3.1). For the viscos-  
 401 ity and the apparent yield stress, power law functions resulted in fits with  $R^2 = 0.99$ . The value  
 402 of  $\beta$  was then calculated from the model ( $\tau_y$ ) and the data ( $G_0$ ) using the relation  $\beta = G_0/\tau_y^2$ .

403

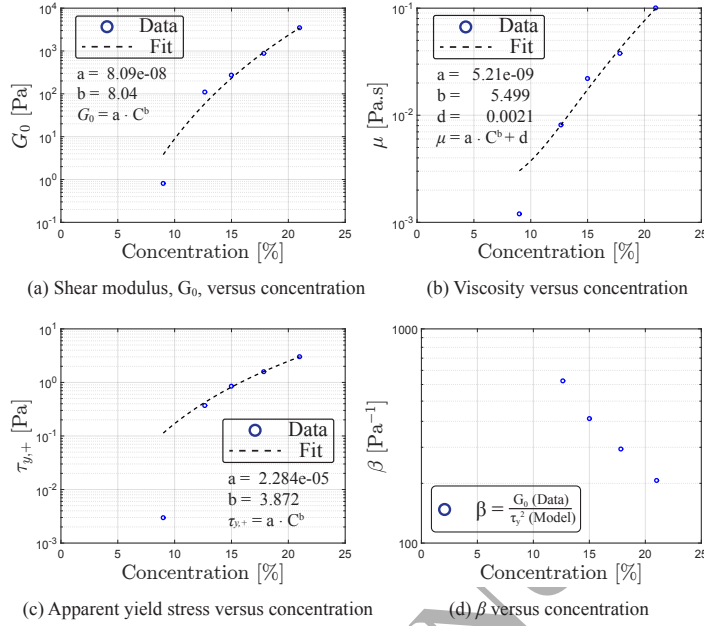


Figure 14: Shear modulus,  $G_0$ , viscosity,  $\mu$ , apparent yield stress  $\tau_{y,+}$ , and  $\beta$  versus sediment volume concentration. The dashed lines are obtained from curve fitting. For the shear modulus, the viscosity, and the apparent yield stress, power law functions resulted in fits with  $R^2 = 0.99$ . The apparent yield stress and shear modulus data obtained from samples with 9% concentration were not considered during fitting.

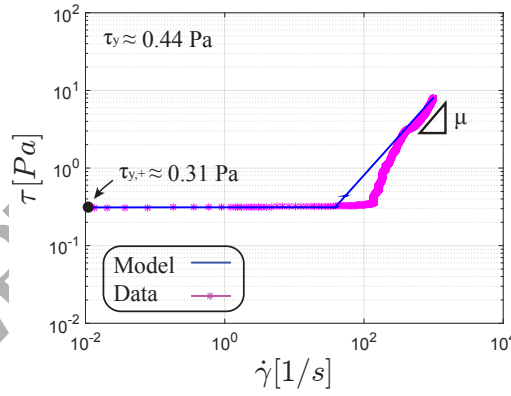


Figure 15: Stress versus strain rate curve obtained from stress controlled measurements after a resting period of 3000 seconds for a representative sample with 12.65% concentration. The solid blue line is computed using equations (23) to (25).

#### 404 3.4. Structure build up rate, $\alpha$

405 From equation (24), for low values of,  $|\tau : \dot{\gamma}|$ , one has,

$$\dot{\lambda} \approx \alpha(1 - \lambda). \quad (30)$$

406 Therefore, in order to obtain the structure build up rate,  $\alpha$ , the value of  $|\tau : \dot{\gamma}|$  should be kept  
 407 small. Furthermore, the imposed stress amplitude must be set such that it is smaller than the  
 408 critical stress,  $\tau_c$ .

409 Immediately after the introduction of the mixture into the cylinder, stress controlled oscillatory  
 410 tests were performed and the change of storage modulus was monitored in time. The amplitude  
 411 of the sinusoidal stress input was set to  $0.002 Pa$  and the angular frequency was set to  $0.5 rad/s$ .  
 412 Figure 16 shows the change of storage modulus in time obtained from the measurements for  
 413 samples with 12.65% and 15% concentrations.

414 To quantify the structure build up rate,  $\alpha$ , equations (23) to (25) were solved. For the computa-  
 415 tions the same input parameters as the rheometry tests were used. The results were then fitted to  
 416 the measurement data. The blue dashed lines in Figure 16 depict the results of this procedure.  
 417 The values of  $\alpha$  obtained from this procedure for the samples with 17.82% and 21% concentra-  
 418 tions were 0.00025 and 0.00015, respectively.

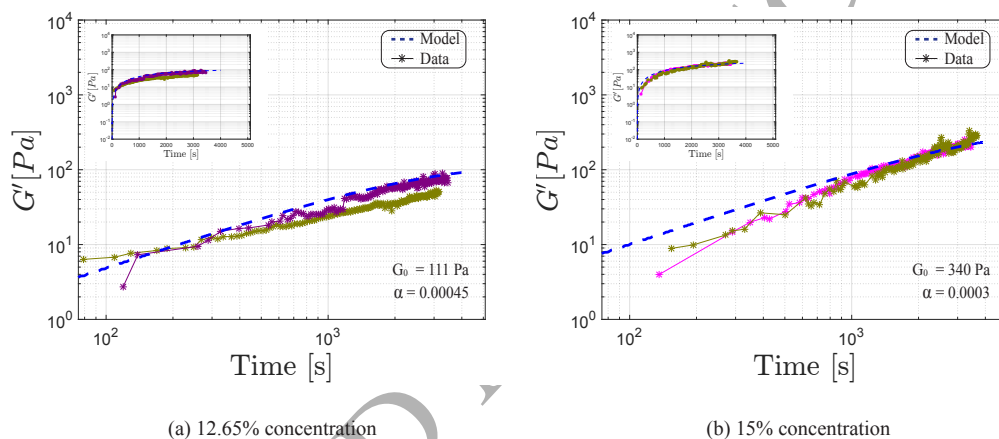


Figure 16: Modeled (blue dashed lines) and measured (purple and green lines) storage modulus,  $G'$ , depicting structure build up in time for (a) 12.65%, and (b) 15% concentrations.

### 419 3.5. Stress controlled measurements

420 A set of measurements were performed on a sample with 15% sediment concentration. In  
 421 order to enhance the reproducibility of the results, before the measurements, the sample was  
 422 pre-sheared. This was done by increasing the stress from  $0.004 Pa$  to  $10 Pa$ , immediately after  
 423 the introduction of the sample within the cylinder geometry. The duration of this phase was  
 424 510 seconds. Next the mixture was left to rest for a period of 9000 seconds to regain structure.  
 425 Subsequently, the stress was increased ramp logarithmically from  $0.004 Pa$  to  $10 Pa$ . Each data  
 426 point was obtained by the rheometer once the shear rate reached a steady state. The mixture  
 427 was then left to rest for a period of 9000 seconds to regain structure. Finally, a stress controlled  
 428 oscillatory test was performed on the mixture. The angular frequency was set to  $0.5 rad/s$  and  
 429 the stress amplitude was increased ramp logarithmically from  $0.004 Pa$  to  $10 Pa$ .

430 For the numerical simulations, the same input conditions as for the measurements were used. For  
 431 the oscillatory amplitude sweep computations, in order to suppress the noise within the numerical  
 432 results, a lowpass filter was used in regions before the yielding occurred, and subsequent to  
 433 yielding, average values of the storage and loss moduli were considered.

### 434 3.6. Strain controlled measurements

435 Strain controlled measurements were performed on a sample with 15% sediment concen-  
 436 tration. Prior to the measurements, the sample was left at rest for a period of 3000 seconds in  
 437 order to regain structure. Subsequently, the strain rate was increased ramp logarithmically from  
 438  $10^{-6}\text{s}^{-1}$  to  $500\text{s}^{-1}$ . The duration for obtaining a data point was set to 2 seconds. The number  
 439 of measurement points was set to 7830. Data reproducibility was considered acceptable to not  
 440 include a pre-shear period. For the numerical simulations, the same input conditions as for the  
 441 measurements were used.

442

## 443 4. Results and discussion

444 In this section first the solutions of equations (23) to (25) for some selected flows is presented.  
 445 Subsequently, the ability of the model to reproduce the results obtained from the stress and the  
 446 strain controlled measurements, discussed in Sections 3.5 and 3.6, is evaluated.

### 447 4.1. Deformation under constant stress

448 We would like to investigate the predictions of the model at the solid-liquid transition. To do  
 449 this we look at, (1) creep tests performed with different stress levels on a completely structured  
 450 material  $\lambda = 1$ , and (2) creep tests performed with a specific stress level on a material with dif-  
 451 ferent initial structure states.

452 Figure 17(a) depicts material deformation as a function of time for a completely structured ma-  
 453 terial,  $\lambda_0 = 1$ , under different stress levels,  $\tau$ , where  $\tau(t) = \tau H(t)$ , and  $H(t)$  is the Heaviside unit  
 454 step function. As it is common place for pasty materials [35], two regimes can be observed. For  
 455 stresses smaller than  $\tau_{y,+}$ , the model predicts an initial rapidly rising phase in the deformation,  
 456 followed by a leveling off and reaching a plateau phase. For stresses higher than  $\tau_{y,+}$ , the model  
 457 predicts a straight line of slope 1 in the logarithmic scale, i.e., the deformation tends to increase  
 458 at a constant rate. It can be seen that the transition between the two regimes is abrupt in terms of  
 459 shear rate, i.e., for a small increase in stress beyond  $\tau_{y,+}$ , the slope of  $\gamma(t)$  changes abruptly from  
 460 zero to 1. As it was explained in section 2.8, the value of  $\tau_{y,+}$  is a function of how fast the stress  
 461 ramp is reached and is smaller than  $\tau_y$  (in this case  $\tau_{y,+} = 0.5\tau_y$ ).

462 Figure 17(b) shows the material deformation as a function of time after application of a stress  
 463 ramp to a material with various initial structure parameters. It can be seen that for an initial  
 464 structure parameter higher than approximately 0.4, the material shows an elastic solid behavior.  
 465 For lower initial structure parameters however, the behavior of the material abruptly transforms  
 466 to that of a viscous liquid.

467 Once stress is applied to a material, its structure is damaged and begins to undergo a recovery  
 468 process known as aging [35]. For very short creep test durations,  $t_w$ , the deformation undergone  
 469 by the material during the test is almost completely recovered for sufficiently long relaxation  
 470 times. For longer creep tests on the other hand, the model predicts a drop in  $\gamma(t)$  to a remaining  
 471 value,  $\gamma_i$ . Figure 18 shows the deformation response of a material, as predicted by the model,  
 472 to creep tests with different test durations,  $t_w$ . It can be seen that for longer  $t_w$ , the value of the  
 473 remaining strain is higher. Once the structure is completely recovered,  $\gamma_i$  converges to a fixed  
 474 value.

475 All these trends have been discussed by Coussot et al. [35] for various pasty materials.

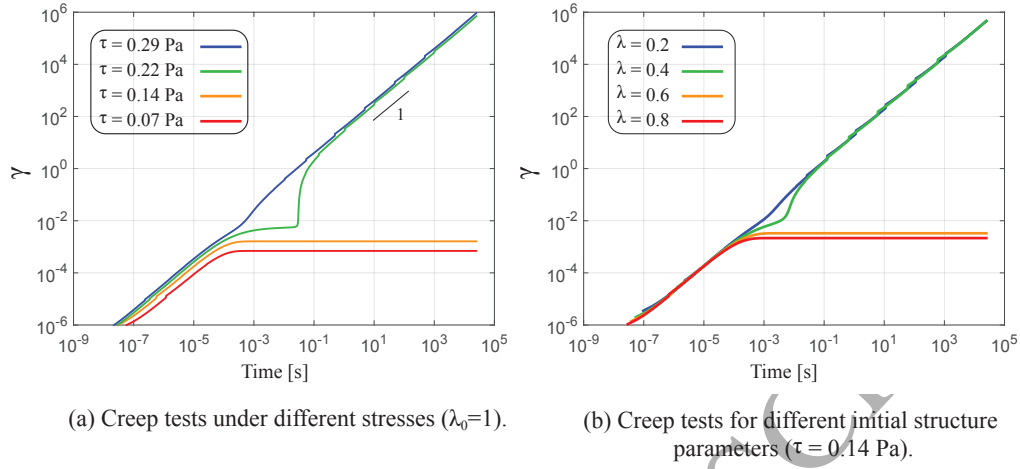


Figure 17: Creep test plots obtained from equations (23) to (25) for (a) a completely structured material,  $\lambda_0 = 1$ , under various stress levels, and (b) for various initial structure states and under a constant stress level,  $\tau = 0.14$  Pa. The value of the yield stress,  $\tau_y$ , was set to 0.37 Pa.

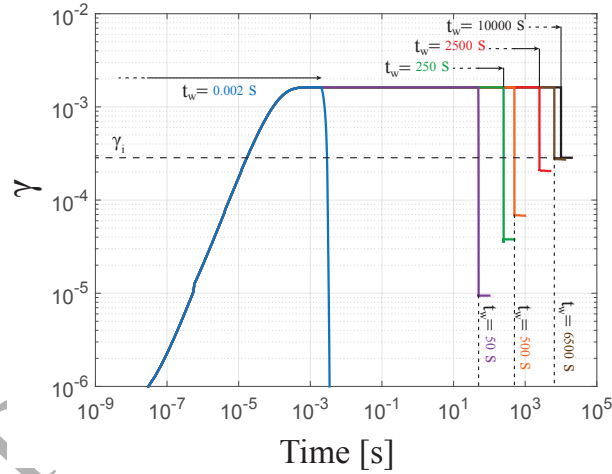


Figure 18: The deformation response of a material obtained from equations (23) to (25) to creep tests with different durations,  $t_w$ . The horizontal dashed line depicts the remaining strain,  $\gamma_i$ , after complete recovery of the material.

#### 4.2. Deformation under constant strain rate

Let  $\dot{\gamma}(t) = \dot{\gamma}(H(t - t_0) - H(t - t_1) + H(t - t_2))$ , where  $t_0$  and  $t_2$  correspond to the times at which a strain rate of magnitude  $\dot{\gamma}$  is applied to a completely structured material, and  $t_1$  corresponds to the cessation of application of strain rate. The stress response of a material to such an input is depicted in Figure 19. For small strain rate inputs (Figure 19(a)), the elastic stress is dominant, i.e.,  $\tau \approx G_0 \zeta$ . In this regime no prominent local maximum can be observed in the stress response at  $t = t_0$  (at which point the strain rate  $\dot{\gamma}$  is initially applied). Instead, the stress increases until it reaches a steady value. Once the strain rate is set to zero at  $t = t_1$ , the stress response shows

484 no change. This indicates that for  $t_0 < t < t_1$ , the material undergoes a deformation in this  
 485 regime that is not recovered once the shear rate is set to zero, i.e., as  $\lambda \rightarrow 1$  for long relaxation  
 486 times,  $\gamma_r$  approaches a constant value. At  $t = t_2$ , again a strain rate of magnitude  $\dot{\gamma}$  is applied  
 487 to the material. The stress response shows an initial increase at  $t = t_2$  to a maximum, drops  
 488 to a minimum, and increases and reaches the same steady value as it had reached just before  
 489  $t = t_1$ . This is because the high shear rate after the jump results in a sudden increase in the  
 490 stress, which then breaks the structure. Since the structure is lost, the stress begins to drop to a  
 491 minimum (inset plot in Figure 19(a)). At this stage the material begins to recover its structure,  
 492 and the stress begins to increase and reach a steady state value. The time it takes the material  
 493 to reach the steady state after  $t = t_2$  is shorter than the time it took it initially to recover after  
 494  $t = t_0$ . This is due to the fact that at  $t = t_2$ ,  $\gamma_r(t_2) > \gamma_r(t_0) = 0$ . Therefore, it takes a shorter time  
 495 for  $\gamma_r$  to reach the steady value, because it is closer to it. The same behavior can be observed in  
 496 Figure 19(b), with the difference that now at  $t = t_0$ , stress responses show clear local maximums  
 497 which are larger than the ones at  $t = t_2$ . This signifies that in this regime the applied strain rate  
 498 is high enough to elicit an elastic response from the material that diffuses for long enough times.  
 499 The red line in Figure 19(c) marks the initiation of a regime where viscous stresses first become  
 500 comparable in magnitude to elastic stresses. Both the red and the yellow lines in this figure show  
 501 a jump at  $t = t_1$ . This is because once the strain rate is set to zero at  $t = t_1$ , the portion of the  
 502 stress response corresponding to viscous stress vanishes, i.e.,  $\mu\dot{\gamma} = 0$ , and only the elastic part  
 503 remains. As viscous stresses become the dominant form of stress at high shear rates the jumps in  
 504 the stress response at  $t = t_1$  become more severe (Figure 19(d)). Another interesting feature that  
 505 can be observed from Figure 19 is that for lower strain rates, the time required to reach a steady  
 506 state increases dramatically [28].  
 507 These trends are corroborated by data for various thixotropic materials in the literature [36, 34].

#### 508 4.3. Stress controlled measurements

509 Figure 20 shows the results of the stress controlled measurements that were described in  
 510 section 3.5.

511 Figure 20(a) presents the stress versus strain rate curves that were obtained from the model (blue  
 512 line) and the measurements (red circles). The values of the empirical parameters used to solve  
 513 the equations (23) to (25) are presented in this figure. The inset plot depicts the stress input,  
 514 corresponding to  $\dot{\gamma} > 10^{-4} \text{ s}^{-1}$ , that was imposed during the measurements and used during  
 515 the simulation. It can be seen that the model shows a good agreement with the data within the  
 516 liquefaction and the fluid regimes.

517 Figure 20(b) shows the stress as a function of strain. At very low values of strain, i.e.,  $\gamma <$   
 518  $10^{-4}$ , the model shows small deviations from the measurements. These deviations did not have  
 519 the same shape for all the sample measurements and sometime were not present. Due to the  
 520 complexity of the mixture under investigation, more examination is required to exactly pinpoint  
 521 the source of this discrepancy. Nonetheless, at low values of strain, i.e., within the linear elastic  
 522 regime, a relatively good agreement between the data and the model can be observed. At the  
 523 end of the linear elastic regime and within the non-linear elastic regime, the model again shows  
 524 some deviations from the data. As before, these deviations were not observed for all the sample  
 525 measurements and their source may be traced back to the small amounts of slip that may have  
 526 occurred during the measurement before yielding. The model shows good agreement with the  
 527 data within the liquefaction and the fluid regimes.

528 Figure 20(c) shows the measured and the computed values of the storage,  $G'$ , and the loss,  
 529  $G''$ , moduli as a function of stress amplitude. A good agreement can be observed between the

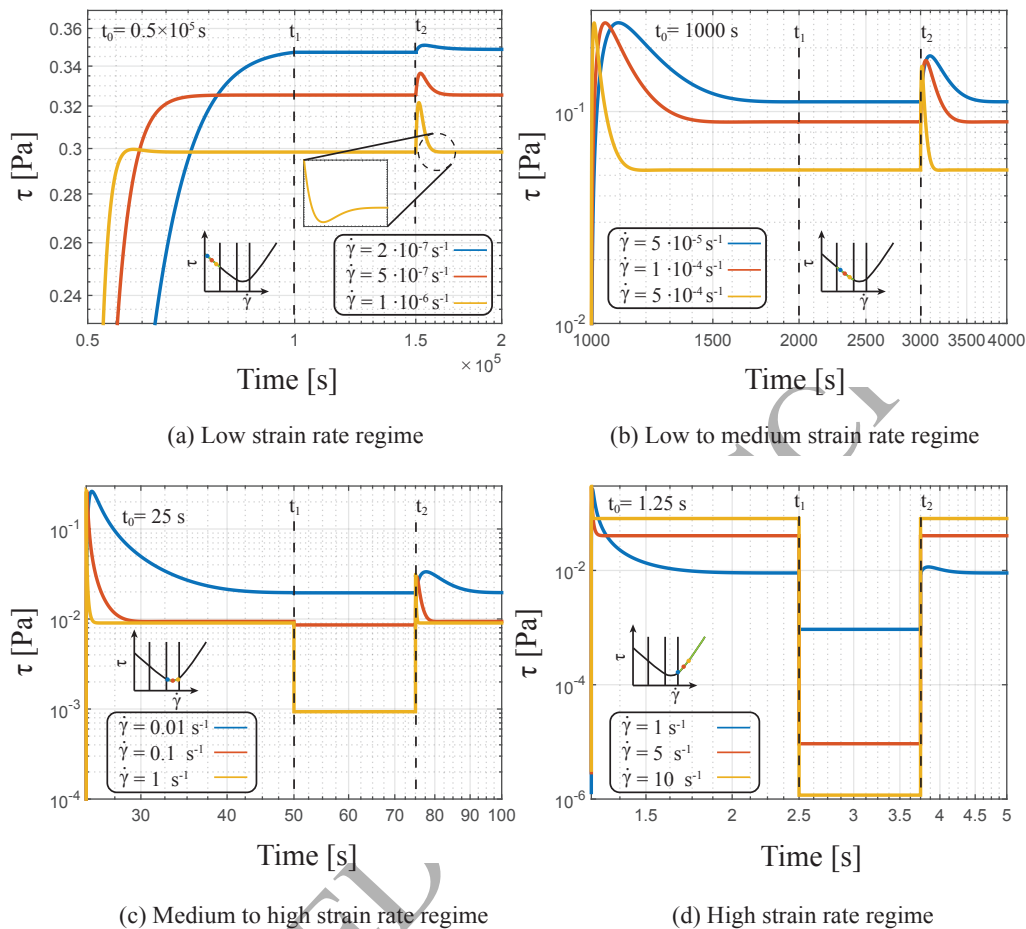


Figure 19: The stress response of a material to the strain rate input  $\dot{\gamma}(t) = \dot{\gamma}(H(t - t_0) - H(t - t_1) + H(t - t_2))$ . Since the steady state was achieved faster at higher shear rates, the duration of the input signal (i.e.  $t_2 - t_0$ ) was varied for the sake of improved visibility. The inset plot shows a schematic strain controlled flow curve and where the constant strain rate lines may fall on such a plot.

530 measured and the computed values of the storage and the loss moduli within the linear and the  
 531 nonlinear elastic regimes. At high stress amplitudes however, the data shows a complex behavior.  
 532 The model does not capture this behavior and underestimates the average values of the storage  
 533 and loss moduli within this region. This may be due to the long duration of these tests which  
 534 may have resulted in water evaporation, and in turn, increased viscosity of the mixture.

#### 535 4.4. Transient strain controlled stress versus strain rate curve

536 Figure 21 shows the measured (blue stars) and the computed (solid red line) strain controlled  
 537 shear stress versus strain rate curves for a sample with 15% concentration. The inset plot depicts  
 538 a zoomed in view of the flow instability that is associated with the shear banding phenomenon.  
 539 As discussed by Pignon et al. [9], the shear rate values provided by the rheometer in this region  
 540 correspond to a very localized or transient flow and are smaller than the actual shear rate values.

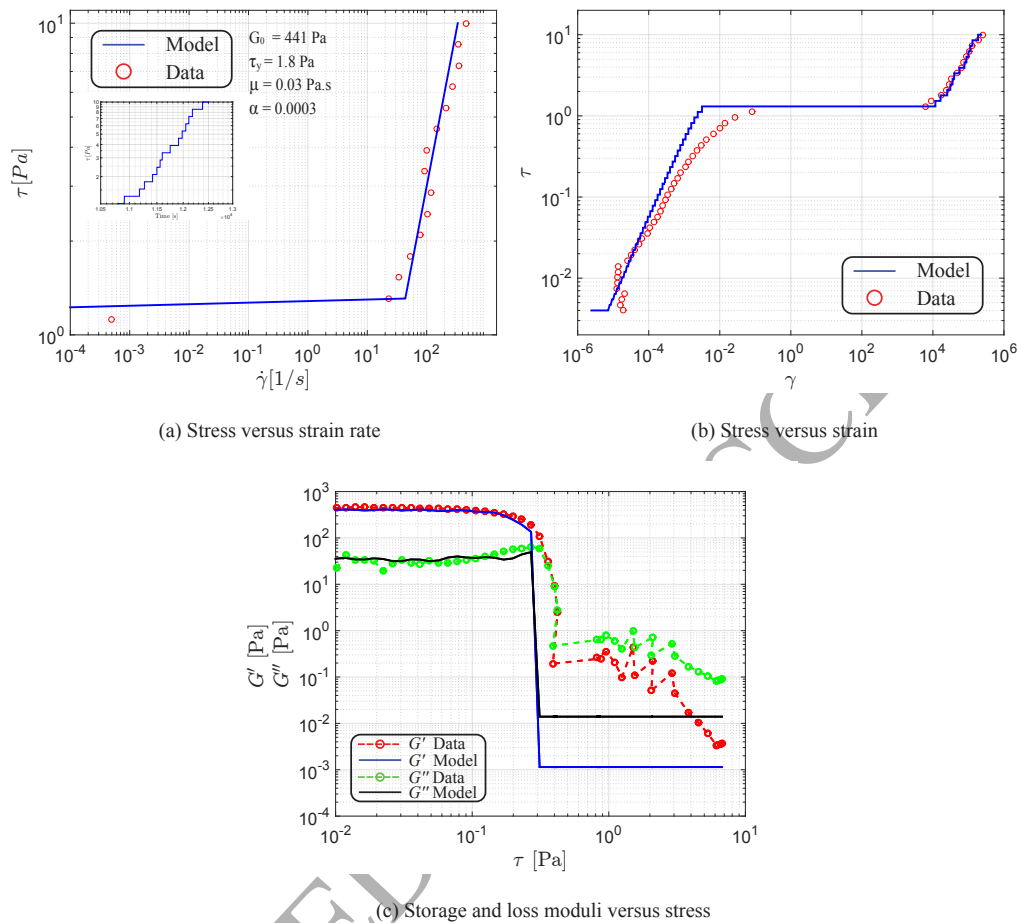


Figure 20: Measured (red and green circles) and computed (solid blue and black lines) stress versus strain rate curve (a), stress versus strain curve (b), and storage and loss moduli versus stress curve (c), obtained from stress controlled measurements for 15% concentration.

541 Therefore, although with the corrected shear rate values, the qualitative shape of the transient  
 542 curve would remain the same, the data in this part of the curve should be precluded from com-  
 543 parison with the model.

544 It can be seen that the measurements and the model both show an initial rise in the shear stress  
 545 until a maximum yield point followed by a drop to a minimum. The measurements suggest that  
 546 at an approximate strain rate of  $10^{-5} \text{ s}^{-1}$  the mixture begins to exhibit strain hardening. The  
 547 model fails to capture this phenomenon. At higher strain rates corresponding to  $\tau > \tau_c$ , the  
 548 measurements and the model begin to again show good agreement.

## 549 5. Conclusions

550 A new viscoelastic constitutive relation for modeling of subaqueous clay-rich gravity flows  
 551 was presented. In order to capture the creep and the yield behavior of the plug layer within

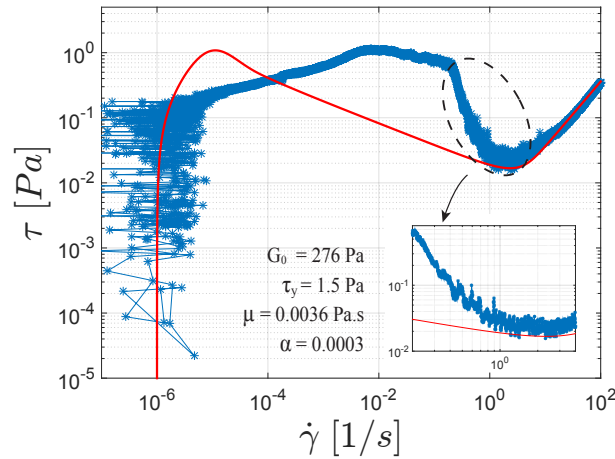


Figure 21: Transient stress versus strain rate curve obtained from strain controlled measurements for a sample with 15% concentration after a resting period of 3000 seconds (blue stars). The solid red line is computed using equations (23) to (25). The value of the empirical parameters used during the computation are presented inside the plot. The inset plot depicts a zoomed in view of the shear banding instability.

552 these flows the Kelvin-Voigt model was considered. The total stress is split into an elastic and a  
 553 viscous part. The importance of the elastic part is determined by the amount of structure. It was  
 554 explained that for the materials which exhibit a minimum in their strain controlled flow curves  
 555 the structure parameter must be a symmetric function of the strain rate and the stress. Therefore,  
 556 the destruction of structure within the material was accounted for using the dissipation energy.  
 557 An expression for the elastic strain of the flowing structure was then derived.

558 It was shown that the final set of equations can reproduce the viscosity bifurcation that clay  
 559 suspensions may exhibit under a given load. This is important for accurate prediction of the  
 560 run-out distance of gravity flows. The most general flow curves which are allowed by the model  
 561 were discussed and the response of the model to a constant stress and a constant shear rate inputs  
 562 was analyzed. It was concluded that the model can reproduce the well documented responses of  
 563 pasty materials to such tests.

564 The final set of equations requires four empirical parameters. A methodology was presented for  
 565 obtaining these parameters. Power law functions were then obtained for their calculations for a  
 566 limited rest time of 3000 seconds.

567 The capability of the model was evaluated by comparing its output with the data obtained from  
 568 stress controlled measurements. At low values of strain, i.e., within the linear elastic regime,  
 569 a relatively good agreement between the data and the model was observed. At the end of the  
 570 linear elastic regime and within the non-linear elastic regime, a discrepancy between the model  
 571 output and the data was observed. This may be due to small amounts of slip that may have  
 572 occurred before yielding. A good agreement between the model and the measurements was  
 573 observed within the yielding and the viscous regions of the stress versus strain and the stress  
 574 versus strain rate curves. For stress controlled oscillatory tests, a good agreement was observed  
 575 between the measured and the computed values of the storage and loss moduli at low stress  
 576 amplitudes. At high stress amplitudes on the other hand, the model appears to deviate from

577 the measurement. This maybe due to the long duration of the tests which may result in water  
 578 evaporation and in turn increased viscosity of the mixture. For transient strain controlled curves,  
 579 a good agreement between the measurements and the model was observed at low and high strain  
 580 rates. The measurements suggest that at intermediate strain rates, the mixture exhibits strain  
 581 hardening. The model does not capture this phenomenon.

## 582 Acknowledgments

583 We would like to thank The Netherlands Research Center For Integrated Solid and Earth Science  
 584 (ISES) for funding this project. We also would like to thank Cor Kasbergen and Dennis den  
 585 Ouden-van der Horst for insightful comments regarding this work.

## 586 Appendix A. Three dimensional formulation of constitutive equation for simple shear flow

587 The expression for the total stress tensor,  $\sigma$ , within a fluid can be written as,

$$\sigma = p\delta + \tau. \quad (\text{A.1})$$

588 where,  $p$  is the thermodynamic pressure,  $\delta$  is the unit tensor, and  $\tau$  is the stress tensor.

589 For isotropic fluids in simple shear flow depicted in Figure A.22, the stress tensor can be written  
 590 as [45, 41],

$$\tau = \begin{pmatrix} \tau^{11} & \tau^{21} & 0 \\ \tau^{21} & \tau^{22} & 0 \\ 0 & 0 & \tau^{33} \end{pmatrix}. \quad (\text{A.2})$$

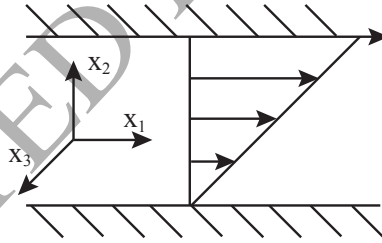


Figure A.22: Simple shear flow.

591 The components of the strain tensor can be written as  $\gamma^{ij} = \delta - g^{ij}$ , where  $g^{ij}$  is the inverse of the  
 592 metric tensor. This yields,

$$\gamma = \begin{pmatrix} -\gamma^{212} & \gamma^{21} & 0 \\ \gamma^{21} & 0 & 0 \\ 0 & 0 & 0 \end{pmatrix}. \quad (\text{A.3})$$

593 The strain rate tensor can be written as,

$$\dot{\gamma} = (\nabla v + \nabla v^T) = \begin{pmatrix} 0 & \dot{\gamma}^{21} & 0 \\ \dot{\gamma}^{21} & 0 & 0 \\ 0 & 0 & 0 \end{pmatrix}. \quad (\text{A.4})$$

594 From the definition of the residual strain and assuming linearity between the stain and the residual  
595 strain tensors yields,

$$\gamma_r^{ks} = \frac{G_{ij}^{-ks} \gamma^{ij}}{\lambda G_0}. \quad (\text{A.5})$$

596 where, the elastic modulus,  $G_{ij}^{-ks}$ , is a fourth-rank tensor.

597 Assuming a homogeneous and isotropic material yields [45],

$$\gamma_r = \begin{pmatrix} \gamma_r^{11} & \gamma_r^{21} & 0 \\ \gamma_r^{21} & \gamma_r^{22} & 0 \\ 0 & 0 & \gamma_r^{22} \end{pmatrix}. \quad (\text{A.6})$$

598 Using the fact that the Christoffel symbols,  $\Gamma_{kl}^i = \frac{1}{2} g^{im} \left( \frac{\partial g_{mk}}{\partial x_l} + \frac{\partial g_{ml}}{\partial x_k} - \frac{\partial g_{kl}}{\partial x_m} \right) = 0$ , and taking the  
599 time derivative of (A.6) and its basis vectors yields [41],

$$\dot{\gamma}_r = \frac{\partial}{\partial t} \begin{pmatrix} \gamma_r^{11} & \gamma_r^{21} & 0 \\ \gamma_r^{21} & \gamma_r^{22} & 0 \\ 0 & 0 & \gamma_r^{22} \end{pmatrix} - \begin{pmatrix} 2\dot{\gamma}^{21} \gamma_r^{21} & \dot{\gamma}^{21} \gamma_r^{22} & 0 \\ \dot{\gamma}^{21} \gamma_r^{22} & 0 & 0 \\ 0 & 0 & 0 \end{pmatrix}. \quad (\text{A.7})$$

600 Finally, the three dimensional formulation of the equations (8) to (10) for the case of the  
601 simple shear flow can be written as,

$$\begin{pmatrix} \tau^{11} & \tau^{21} & 0 \\ \tau^{21} & \tau^{22} & 0 \\ 0 & 0 & \tau^{33} \end{pmatrix} = G_0 \lambda \begin{pmatrix} \gamma_r^{11} & \gamma_r^{21} & 0 \\ \gamma_r^{21} & \gamma_r^{22} & 0 \\ 0 & 0 & \gamma_r^{22} \end{pmatrix} + \mu \begin{pmatrix} 0 & \dot{\gamma}^{21} & 0 \\ \dot{\gamma}^{21} & 0 & 0 \\ 0 & 0 & 0 \end{pmatrix}, \quad (\text{A.8})$$

$$\dot{\lambda} = \alpha(1 - \lambda) - |\tau : \dot{\gamma}| \beta \lambda, \quad (\text{A.9})$$

$$\begin{aligned} \frac{\partial}{\partial t} \begin{pmatrix} \gamma_r^{11} & \gamma_r^{21} & 0 \\ \gamma_r^{21} & \gamma_r^{22} & 0 \\ 0 & 0 & \gamma_r^{22} \end{pmatrix} &= \begin{pmatrix} 2\dot{\gamma}^{21} \gamma_r^{21} & \dot{\gamma}^{21} \gamma_r^{22} & 0 \\ \dot{\gamma}^{21} \gamma_r^{22} & 0 & 0 \\ 0 & 0 & 0 \end{pmatrix} + \begin{pmatrix} 0 & \dot{\gamma}^{21} & 0 \\ \dot{\gamma}^{21} & 0 & 0 \\ 0 & 0 & 0 \end{pmatrix} \\ &- \frac{(1 - \lambda)\alpha}{\lambda} \begin{pmatrix} \gamma_r^{11} & \gamma_r^{21} & 0 \\ \gamma_r^{21} & \gamma_r^{22} & 0 \\ 0 & 0 & \gamma_r^{22} \end{pmatrix}. \end{aligned} \quad (\text{A.10})$$

## 602 Appendix B. Three dimensional formulation of constitutive equation for vortex flow

603 Within the free shear layer, let us consider a vortex flow in the polar coordinates given by,

$$\vec{u} = (v_r, v_\theta, v_z) = \left( 0, \frac{C}{r}, 0 \right), \quad (\text{B.1})$$

604 where,  $C$  is a constant and  $r$  is the distance from the center of the vortex.

605 Using the rotational symmetry of vortex flow, the stress tensor in polar coordinates can be written  
606 as,

$$\tau = \begin{pmatrix} \tau^{11} & 0 & 0 \\ 0 & \tau^{11} & 0 \\ 0 & 0 & \tau^{33} \end{pmatrix}. \quad (\text{B.2})$$

607 The strain tensor can be written as,

$$\gamma = \begin{pmatrix} 0 & -\frac{2Ct}{r^2} & 0 \\ -\frac{2Ct}{r^2} & -\frac{2Ct}{r} & 0 \\ 0 & 0 & 0 \end{pmatrix}. \quad (\text{B.3})$$

608 and the strain rate tensor can be written as,

$$\dot{\gamma} = \begin{pmatrix} 0 & -\frac{2C}{r^2} & 0 \\ -\frac{2C}{r^2} & 0 & 0 \\ 0 & 0 & 0 \end{pmatrix}. \quad (\text{B.4})$$

609 From the definition of the residual strain and assuming linearity between the stain and the  
610 residual strain tensors and a homogeneous, isotropic, material yields,

$$\gamma_r = \begin{pmatrix} \gamma_r^{11} & \gamma_r^{21} & 0 \\ \gamma_r^{21} & \gamma_r^{22} & 0 \\ 0 & 0 & \gamma_r^{33} \end{pmatrix}. \quad (\text{B.5})$$

611 Time derivative of (B.5) can be written as,

$$\dot{\gamma}_r = \frac{\partial}{\partial t} \begin{pmatrix} \gamma_r^{11} & \gamma_r^{21} & 0 \\ \gamma_r^{21} & \gamma_r^{22} & 0 \\ 0 & 0 & \gamma_r^{33} \end{pmatrix} + \begin{pmatrix} -2C\gamma_r^{21} & -C\gamma_r^{22} & 0 \\ -C\gamma_r^{22} & 0 & 0 \\ 0 & 0 & 0 \end{pmatrix}. \quad (\text{B.6})$$

612 Finally, the three dimensional formulation of the equations (8) to (10) for the case of the  
613 vortex flow can be written as,

$$\begin{pmatrix} \tau^{11} & 0 & 0 \\ 0 & \tau^{11} & 0 \\ 0 & 0 & \tau^{33} \end{pmatrix} = G_0 \lambda \begin{pmatrix} \gamma_r^{11} & \gamma_r^{21} & 0 \\ \gamma_r^{21} & \gamma_r^{22} & 0 \\ 0 & 0 & \gamma_r^{33} \end{pmatrix} + \mu \begin{pmatrix} 0 & -\frac{2C}{r^2} & 0 \\ -\frac{2C}{r^2} & 0 & 0 \\ 0 & 0 & 0 \end{pmatrix}, \quad (\text{B.7})$$

$$\lambda = \alpha(1 - \lambda) - |\tau : \dot{\gamma}| \beta \lambda, \quad (\text{B.8})$$

$$\begin{aligned} \frac{\partial}{\partial t} \begin{pmatrix} \gamma_r^{11} & \gamma_r^{21} & 0 \\ \gamma_r^{21} & \gamma_r^{22} & 0 \\ 0 & 0 & \gamma_r^{33} \end{pmatrix} &= \begin{pmatrix} 2C\gamma_r^{21} & C\gamma_r^{22} & 0 \\ C\gamma_r^{22} & 0 & 0 \\ 0 & 0 & 0 \end{pmatrix} + \begin{pmatrix} 0 & -\frac{2C}{r^2} & 0 \\ -\frac{2C}{r^2} & 0 & 0 \\ 0 & 0 & 0 \end{pmatrix} \\ &- \frac{(1 - \lambda)\alpha}{\lambda} \begin{pmatrix} \gamma_r^{11} & \gamma_r^{21} & 0 \\ \gamma_r^{21} & \gamma_r^{22} & 0 \\ 0 & 0 & \gamma_r^{33} \end{pmatrix}. \end{aligned} \quad (\text{B.9})$$

## 614 References

- 615 [1] M. L. Baker, J. H. Baas, J. Malarkey, R. Silva Jacinto, M. J. Craig, I. A. Kane, S. Barker, The Effect of Clay Type  
616 On The Properties of Cohesive Sediment Gravity Flows And Their Deposits, *Jornal of Sedimentary Research* 87  
617 (2017) 1176–1195. doi:10.2110/jsr.2017.63.
- 618 [2] T. Healy, Y. Wang, J. A. Healy, *Muddy Coasts of the World: Processes, Deposits and Function*, Proceedings in  
619 Marine Science, Elsevier Science, 2002.
- 620 [3] J. C. Winterwerp, W. G. M. van Kesteren, *Introduction to the Physics of Cohesive Sediment in the Marine Envi-*  
621 *ronment*, Elsevier, 2004.
- 622 [4] D. S. Van Maren, J. C. Winterwerp, Z. Y. Wang, Q. Pu, Suspended sediment dynamics and morphodynamics in the  
623 Yellow River, China, *Sedimentology* 56 (3) (2009) 785–806. doi:10.1111/j.1365-3091.2008.00997.x.

- 624 [5] P. Coussot, N. Roussel, S. Jarny, H. Chanson, Continuous or catastrophic solid-liquid transition in jammed systems,  
625 *Physics of Fluids* 17 (1). doi:10.1063/1.1823531.
- 626 [6] J. H. Baas, J. L. Best, J. Peakall, Predicting bedforms and primary current stratification in cohesive mixtures of  
627 mud and sand, *Journal of the Geological Society* 173 (1) (2016) 12–45. doi:10.1144/jgs2015-024.
- 628 [7] P. Coussot, Q. D. Nguyen, H. T. Huynh, D. Bonn, Avalanche behavior in yield stress fluids, *Physical Review Letters*  
629 88 (17) (2002) 1755011–1755014. doi:10.1103/PhysRevLett.88.175501.
- 630 [8] P. Coussot, Q. D. Nguyen, H. T. Huynh, D. Bonn, Viscosity bifurcation in thixotropic, yielding fluids, *Journal of*  
631 *Rheology* 46 (3) (2002) 573–589. doi:10.1122/1.1459447.
- 632 [9] F. Pignon, A. Magnin, J.-M. Piau, Thixotropic colloidal suspensions and flow curves with minimum: Identification  
633 of flow regimes and rheometric consequences, *Journal of Rheology* 40 (1996) 573–587. doi:10.1122/1.550759.
- 634 [10] N. Hermidas, J. T. Eggenhuisen, R. Silva Jacinto, S. M. Luthi, F. Toth, F. Pohl, A Classification of  
635 Clay-Rich Subaqueous Density Flow Structures, *Journal of Geophysical Research* 123 (5) (2018) 945–966.  
636 doi:10.1002/2017JF004386.
- 637 [11] A. S. Michaels, J. C. Bolger, Settling rates and sediment volumes of flocculated kaolin suspensions, *Industrial and*  
638 *Engineering Chemistry Fundamentals* 1 (1) (1962) 24–33. doi:10.1021/i160001a004.
- 639 [12] J. Billingham, J. W. J. Ferguson, Laminar, unidirectional flow of a thixotropic fluid in a circular pipe, *Journal of*  
640 *Non-Newtonian Fluid Mechanics* 47 (1993) 21–55. doi:10.1016/0377-0257(93)80043-B.
- 641 [13] C. F. Goodeve, A General Theory of Thixotropy and Viscosity, *Trans. Faraday Soc.* 35 (1939) 342–358.  
642 doi:10.1039/TF9393500342.
- 643 [14] F. Moore, The rheology of ceramic slips and bodies, *Transactions of the British Ceramic Society* 58 (1959) 470–  
644 494.
- 645 [15] S. J. Hahn, T. Ree, H. Eyring, Flow Mechanism of Thixotropic Substances, *Industrial and Engineering Chemistry*  
646 51 (7) (1959) 856–857. doi:10.1021/ie50595a038.
- 647 [16] S. Peter, Zur Theorie der Rheopexie, *Rheologica Acta* 3 (1964) 178–180. doi:10.1007/BF01668885.
- 648 [17] R. S. Rivlin, The hydrodynamics of non-Newtonian fluids. I, *Proceedings of the Royal Society* 193 (1033) (1948)  
649 260–281. doi:10.1098/rspa.1948.0044.
- 650 [18] R. S. Rivlin, The hydrodynamics of non-Newtonian fluids . II, *proceedings of cambridge philosophical society*  
651 45 (1) (1949) 88–91. doi:10.1017/S0305004100000463.
- 652 [19] D. C.-H. Cheng, F. Evans, Phenomenological characterization of the rheological behaviour of inelastic reversible  
653 thixotropic and antithixotropic fluids, *British Journal of Applied Physics* 16 (1965) 1599–1617. doi:10.1088/0508-  
654 3443/16/11/301.
- 655 [20] D. Hewitt, N. Balmforth, Thixotropic gravity currents, *Journal of Fluid Mechanics* 727 (2013) 56–82.  
656 doi:10.1017/jfm.2013.235.
- 657 [21] E. a. Toorman, Modelling the thixotropic behaviour of dense cohesive sediment suspensions, *Rheologica Acta* 36  
658 (1997) 56–65. doi:10.1007/BF00366724.
- 659 [22] C. J. Dimitriou, G. H. McKinley, A comprehensive constitutive law for waxy crude oil: A thixotropic yield stress  
660 fluid, *Soft Matter* 10 (35) (2014) 6619–6644. doi:10.1039/c4sm00578c.
- 661 [23] D. Acierno, F. La Mantia, G. Marrucci, G. Titomanlio, A non-linear viscoelastic model with structure-dependent re-  
662 laxation times, *Journal of Non-Newtonian Fluid Mechanics* 1 (1976) 125–146. doi:10.1016/0377-0257(76)80012-  
663 2.
- 664 [24] P. Coussot, A. I. Leonov, J. M. Piau, Rheology of concentrated dispersed systems in a low molecular weight matrix,  
665 *Journal of Non-Newtonian Fluid Mechanics* 46 (1993) 179–211. doi:10.1016/0377-0257(93)85046-D.
- 666 [25] D. De Kee, C. F. Chan Man Fong, Rheological properties of structured fluids, *Polymer Engineering & Science*  
667 34 (5) (1994) 438–445. doi:10.1002/pen.760340510.
- 668 [26] C. F. C. M. Fong, G. Turcotte, D. De Kee, Modelling Steady and Transient Rheological Properties, *Journal of Food*  
669 *Engineering* 27 (1996) 63–70. doi:10.1016/0260-8774(94)00077-M.
- 670 [27] F. Yziquel, P. J. Carreau, M. Moan, P. A. Tanguy, Rheological modeling of concentrated colloidal suspensions,  
671 *Journal of Non-Newtonian Fluid Mechanics* 86 (1999) 133–155. doi:10.1016/S0377-0257(98)00206-7.
- 672 [28] P. R. de Souza Mendes, Modeling the thixotropic behavior of structured fluids, *Journal of Non-Newtonian Fluid*  
673 *Mechanics* 164 (1-3) (2009) 66–75. doi:10.1016/j.jnnfm.2009.08.005.
- 674 [29] P. Sollich, P. Hébraud, M. E. Cates, Rheology of Soft Glassy Materials, *Physical Review Letters* 78 (10).  
675 doi:10.1103/PhysRevLett.78.2020.
- 676 [30] S. M. Fielding, P. Sollich, M. E. Cates, Ageing and Rheology in Soft Materials, *Journal of Rheology* 44 (2).  
677 doi:10.1122/1.551088.
- 678 [31] M. L. Falk, J. S. Langer, Dynamics of viscoplastic deformation in amorphous solids, *Physical Review E* 57 (6)  
679 (1998) 7192–7205. doi:10.1103/PhysRevE.57.7192.
- 680 [32] L. Bocquet, A. Colin, A. Ajdari, Kinetic theory of plastic flow in soft glassy materials, *Physical Review Letters*  
681 103 (3) (2009) 1–4. doi:10.1103/PhysRevLett.103.036001.
- 682 [33] A. Mujumdar, A. N. Beris, A. B. Metzner, Transient phenomena in thixotropic systems, *Journal of Non-Newtonian*

- 683 Fluid Mechanics 102 (2002) 157–178. doi:10.1016/s0377-0257(01)00176-8.
- 684 [34] K. Dullaert, J. Mewis, A structural kinetics model for thixotropy, *Journal of Non-Newtonian Fluid Mechanics* 139  
685 (2006) 21–30. doi:10.1016/j.jnnfm.2006.06.002.
- 686 [35] P. Coussot, H. Tabuteau, X. Chateau, L. Tocquer, G. Ovarlez, Aging and solid or liquid behavior in pastes, *Journal*  
687 *of Rheology* 50 (6) (2006) 975–994. doi:10.1122/1.2337259.
- 688 [36] C. Derec, G. Ducouret, A. Ajdari, F. Lequeux, Aging and nonlinear rheology in suspensions of polyethylene  
689 oxideprotected silica particles, *Physical Review E* 67 (6) (2003) 9. doi:10.1103/PhysRevE.67.061403.
- 690 [37] H. V. Olphen, *An introduction to clay colloid chemistry: for clay technologists, geologists, and soil scientists*,  
691 Wiley, 1977.
- 692 [38] P. Coussot, *Mudflow Rheology and Dynamics*, IAHR Monographs, Taylor & Francis, 1997.
- 693 [39] R. Roscoe, Mechanical Models for the Representation of Visco-Elastic Properties, *British Journal of Applied*  
694 *Physics* 1 (7) (1950) 171–173. doi:10.1088/0508-3443/1/7/302.
- 695 [40] R. Mas, A. Magnin, Rheology of colloidal suspensions: Case of lubricating greases, *Journal of Rheology* 38 (4)  
696 (1994) 889–908. doi:10.1122/1.550598.
- 697 [41] R. B. Bird, R. C. Armstrong, O. Hassager, *Dynamics of Polymeric Liquids*, 2nd Edition, John Wiley & Sons, 1987.
- 698 [42] G. C. Holmes, The Use of Hyperbolic Cosines in Solving Cubic Polynomials, *The Mathematical Gazette* 86 (507)  
699 (2002) 473–477. doi:10.2307/3621149.
- 700 [43] A. S. Yoshimura, R. K. Prud'homme, Response of an elastic Bingham fluid to oscillatory shear, *Rheologica Acta*  
701 26 (5) (1987) 428–436. doi:10.1007/BF01333843.
- 702 [44] L. F. Shampine, M. W. Reichelt, The MATLAB ODE Suite, *SIAM Journal on Scientific Computing* 18 (1) (1997)  
703 1–22. doi:10.1137/S1064827594276424.
- 704 [45] R. I. Tanner, *Engineering Rheology*, Oxford Engineering Science Series, OUP Oxford, 2000.